Title

The influence of seawater carbonate chemistry, mineralogy, and diagenesis on calcium isotope variations in Lower-Middle Triassic carbonate rocks

Permalink

https://escholarship.org/uc/item/6v0262wf

Journal

Chemical Geology, 471

ISSN

0009-2541

Authors

Lau, KV
Maher, K
Brown, ST
et al.

Publication Date

2017-11-05

DOI

10.1016/j.chemgeo.2017.09.006

Peer reviewed

The influence of seawater carbonate chemistry, mineralogy, and diagenesis on calcium isotope variations in Lower-Middle Triassic carbonate rocks

Kimberly V. Lau[a,1], Kate Maher[a], Shaun T. Brown[b,c], Adam B. Jost[a,d], Demir Altıner[e], Donald J. DePaolo[b,c], Anton Eisenhauer[r], Brian M. Kelley[a,g], Daniel J. Lehrmann[h], Adina Paytan[i], Juan Carlos Silva-Tamayo[a,j], Meiyi Yu[k], and Jonathan L. Payne[a]

[a]Department of Geological Sciences, Stanford University, 450 Serra Mall Bldg. 320, Stanford, CA 94305, USA.
[b]Department of Earth and Planetary Science, University of California, Berkeley, 307 McCone Hall, Berkeley, CA 94709, USA.
[c]Energy Geosciences Division, E.O. Lawrence Berkeley National Laboratory, 1 Cyclotron Road, Berkeley, CA 94720, USA.
[d]Department of Earth, Atmospheric, and Planetary Sciences, Massachusetts Institute of Technology, 77 Massachusetts Ave., Cambridge, MA 02139.
[e]Department of Geological Engineering, Middle East Technical University, Üniversiteler Mah. Dumlupınar Blv. No: 1,06800, 06531, Ankara, Turkey.
[f]GEOMAR, Helmholtz Centre for Ocean Research Kiel, Wischhofstr. 1-3, 24148 Kiel, Germany.
[g]ExxonMobil Upstream Research Company, 22777 Springwoods Village Parkway, Spring, TX 77389.
[h]Geosciences Department, Trinity University, Marrs McLean Hall, One Trinity Place, San Antonio, TX 78212, USA.
[i]Institute of Marine Sciences, University of California, Santa Cruz, 1156 High Street, Santa Cruz, CA 95064 USA.
[j]TESTLAB Geo-Ambiental, Kra 45D #60-16, Medellin, Colombia.
[k]College of Resource and Environment Engineering, Guizhou University, Caijiaguan, Guiyang 550003, Guizhou, China.

[1]corresponding author (kvlau@ucr.edu). Present address: Department of Earth Sciences, University of California, Riverside, 900 University Avenue, Riverside, CA 92521, USA.

Keywords: calcium isotopes; carbonates; early diagenesis; recrystallization; calcium cycling

ABSTRACT

The geological calcium cycle is linked to the geological carbon cycle through the weathering and burial of carbonate rocks. As a result, calcium (Ca) isotope ratios ($^{44}Ca/^{40}Ca$, expressed as $\delta^{44/40}Ca$) can help to constrain ancient carbon cycle dynamics if Ca cycle behavior can be reconstructed. However, the $\delta^{44/40}Ca$ of carbonate rocks is influenced not only by the $\delta^{44/40}Ca$ of seawater but also by diagenetic processes and fractionation associated with carbonate precipitation. In this study, we investigate the dominant controls on carbonate $\delta^{44/40}Ca$ in Upper Permian to Middle Triassic limestones (ca. 253 to 244 Ma) from south China and Turkey. This time interval is ideal for assessing controls on Ca isotope ratios in carbonate rocks because fluctuations in seawater $\delta^{44/40}Ca$ may be expected based on several large carbon isotope ($\delta^{13}C$) excursions ranging from -2 to +8‰. Parallel negative $\delta^{13}C$ and $\delta^{44/40}Ca$ excursions were previously identified across the end-Permian extinction horizon. Here, we find a second negative excursion in $\delta^{44/40}Ca$ of ~0.2‰ within Lower Triassic strata in both south China and Turkey; however, this excursion is not synchronous between regions and thus cannot be interpreted to reflect secular change in the $\delta^{44/40}Ca$ of global seawater. Additionally, $\delta^{44/40}Ca$ values from Turkey are consistently 0.3‰ lower than contemporaneous samples from south China, providing further support for local or regional influences. By measuring $\delta^{44/40}Ca$ and Sr concentrations ([Sr]) in two stratigraphic sections located at opposite margins of the Paleo-Tethys Ocean, we can determine whether the data represent global conditions (*e.g.*, secular variations in the $\delta^{44/40}Ca$ of seawater) versus local controls (*e.g.*, original mineralogy or diagenetic alteration). The [Sr] and $\delta^{44/40}Ca$ data from this study are best described statistically by a log-linear correlation that also exists in many previously published datasets of various geological ages. Using a model of early marine diagenetic water-rock interaction, we illustrate that this general correlation can be explained by the chemical evolution of bulk carbonate sediment samples with different initial mineralogical compositions that subsequently underwent recrystallization. Although early diagenetic resetting and carbonate mineralogy strongly influence the carbonate $\delta^{44/40}Ca$ values, the relationship between [Sr] and $\delta^{44/40}Ca$ holds potential for reconstructing first-order secular changes in seawater $\delta^{44/40}Ca$ composition.

1. INTRODUCTION

Records of calcium isotopes ($\delta^{44/40}$Ca), measured in marine carbonate rocks, fossils, and authigenic minerals, provide important constraints on global calcium (Ca) and carbon © cycle dynamics over the past billion years (*e.g.*, Blättler et al., 2011; Brazier et al., 2015; De La Rocha and DePaolo, 2000; Du Vivier et al., 2015; Fantle and DePaolo 2005; Farkaš et al., 2007 and 2016; Gothmann et al., 2016; Griffith et al., 2008 and 2011; Holmden et al., 2009 and 2012a; Husson et al., 2015; Jost et al., 2014 and 2017; Kasemann et al., 2014; Payne et al., 2010; Sawaki et al., 2014; Silva-Tamayo et al., 2010a and 2010b). Seawater $\delta^{44/40}$Ca may reflect coupled C and Ca cycling because its value is controlled by the balance between the major Ca input, continental weathering, and the major Ca output, $CaCO_3$ burial (De La Rocha and DePaolo, 2000; DePaolo, 2004; Fantle and DePaolo, 2005). During $CaCO_3$ precipitation, Ca is fractionated such that ^{40}Ca is preferentially incorporated into carbonate minerals, enriching seawater in ^{44}Ca relative to the riverine input (*e.g.*, DePaolo, 2004). Assuming that riverine $\delta^{44/40}$Ca does not vary significantly across time, the $\delta^{44/40}$Ca record of carbonate sediments could reflect changes in carbonate mineralogy or the sedimentation flux. If the carbonate burial flux increases due to higher alkalinity (with no contemporaneous changes in hydrothermal input or groundwater flux), seawater $\delta^{44/40}$Ca also increases. On the other hand, if carbonate saturation state (Ω) decreases temporarily in an acidified ocean, reduced carbonate sedimentation results in a transient decrease in seawater $\delta^{44/40}$Ca (Payne et al., 2010). In this study, we examine the potential for Ca isotopes, as recorded in carbonate rocks, to provide insight into the coupled C and Ca cycles by focusing on Lower to Middle Triassic carbonate strata from stratigraphic sections located in south China and Turkey.

Carbonate $\delta^{44/40}$Ca records can provide constraints on marine C and Ca cycling if variations in these data reflect variations in seawater $\delta^{44/40}$Ca. Calcium isotopes are readily analyzed in bulk carbonate rock, an approach that is useful for time intervals prior to the Cenozoic that are not represented in the deep-sea sediment record. However, various factors can affect the extent to which the $\delta^{44/40}$Ca composition of bulk carbonate rock tracks seawater at the time of deposition. The kinetic fractionation of Ca isotopes during precipitation of $CaCO_3$ from seawater ($\Delta_{\text{carbonate-seawater}}$, hereafter $\Delta_{\text{c-s}}$) is likely controlled by reaction rate, mineralogy, and fluid stoichiometry (DePaolo, 2004; Fantle and DePaolo, 2005; Fantle et al., 2010; Gussone et al., 2005; Nielsen et al., 2012; Sime et al., 2007; Skulan et al., 1997; Tang et al., 2008a). Some of these factors can vary globally and across geologic time through changes in biology and ocean chemistry (*e.g.*, Blättler et al., 2012; Farkaš et al., 2007), whereas others vary at limited spatial scales. The $\delta^{44/40}$Ca of shallow-marine carbonates may also be influenced by mixing with groundwater or altered by post-depositional interaction with diagenetic fluids (Fantle, 2015; Fantle and Higgins, 2014; Holmden, 2009; Holmden et al., 2012b). Therefore, many factors must be considered before interpreting the carbonate $\delta^{44/40}$Ca record as secular changes in seawater $\delta^{44/40}$Ca.

The Early to Middle Triassic recovery from the end-Permian mass extinction is an ideal time interval in which to examine the controls on the $\delta^{44/40}$Ca of carbonate rocks because there is ample evidence for large perturbations in the global C and Ca cycles. The end-Permian catastrophe (ca. 252 Ma), the largest mass extinction of the Phanerozoic, was likely triggered by a large and rapid release of C from the emplacement of the Siberian Traps, resulting in acidification, anoxia, and warming coincident with the loss of ~80% of marine genera (reviewed in Payne and Clapham, 2012). Large fluctuations in the carbon cycle characterized the five million years after the end-Permian mass extinction: Early Triassic δ^{13}C values exhibit multiple negative (down to approximately -2‰) and positive (up to approximately 8‰) excursions (Atudorei, 1999; Horacek et al., 2007a; Horacek et al., 2007b; Payne et al., 2004; Richoz, 2006), and did not fully stabilize until the Middle Triassic. Biodiversity, ecological complexity, and body size also did not return to pre-extinction levels until the Middle Triassic, suggesting that adverse conditions extended beyond the initial extinction event (*e.g.*, Brayard et al., 2006; Brayard et al., 2009; Chen and Benton, 2012; Foster and Twitchett, 2014; Hallam, 1991; Orchard, 2007; Schaal et al., 2016; Stanley, 2009). Because $\delta^{44/40}$Ca data can be collected from the same samples as those used to determine variations in δ^{13}C, this time interval serves as an important test case for the utility of $\delta^{44/40}$Ca data in carbonate rocks for reconstructing seawater $\delta^{44/40}$Ca, as well as for elucidating links between the Early-Middle Triassic Ca and C cycles.

At the Permian/Triassic boundary, the globally observed negative δ^{13}C excursion is commonly attributed to a release of ^{13}C-depleted CO_2 during Siberian Traps volcanism and volatilization of C-rich sediments (*e.g.*, Cui et al., 2013; Svensen et al., 2009). Because rapidly elevated atmospheric pCO_2 would increase Ca weathering as well as decrease the burial rate of $CaCO_3$, a negative excursion in $\delta^{44/40}$Ca that parallels this negative δ^{13}C excursion was interpreted as evidence for a major episode of ocean acidification (Hinojosa et al., 2012; Payne et al., 2010). A number of additional lines of evidence support an end-Permian acidification event, including high ^{187}Re/^{188}Os ratios in shales (Georgiev et al., 2011), the paleophysiology of animals that were most severely impacted (Clapham and Payne, 2011; Kiessling and Simpson, 2011; Knoll et al., 2007), sedimentological observations such as dissolution surfaces and subsequent abiotic carbonate precipitation (Baud et al., 2007; Payne et al., 2007; Pruss et al., 2006; Weidlich and Bernecker, 2011; Woods et al., 1999; Woods, 2014), and a negative boron isotope excursion that suggests a short-lived acidification event (Clarkson et al., 2015).

In contrast to the boundary δ^{13}C excursion, the causes of Early Triassic δ^{13}C instability are widely debated. The large negative and positive δ^{13}C excursions that characterize the remainder of the Early Triassic have been interpreted to represent several pulses of volcanic C release (Payne and Kump, 2007). However, radiometric dates of Siberian Traps rocks indicate that magmatism greatly diminished within 0.5 Ma of the main extinction pulse (Burgess and Bowring, 2015), suggesting that volcanic pulses are unlikely to have continued for 5 Ma. Nonetheless, evidence from sedimentology and paleoredox proxies support variations in Ω of the Early Triassic oceans. Microbialites and aragonite fan pseudomorphs—representative of supersaturated oceans with high Ω—occur in localities throughout the Tethys and the eastern Panthalassa margin that span the Permian/Triassic boundary through the Early Triassic (Baud et al., 2007; Pruss et al., 2006; Weidlich and Bernecker, 2011; Woods et al., 1999). Widespread abiotic $CaCO_3$ precipitation, particularly in deeper waters, is characteristic of an extensively anoxic ocean (Lau et al., 2016; Song et al., 2014) dominated by anaerobic metabolisms that increase alkalinity and authigenic carbonate precipitation at or below the sediment-water interface (SWI) (Bergmann et al., 2013; Higgins et al., 2009; Loyd et al., 2012; Maher et al., 2006; Woods, 2014). Early Triassic C and uranium (U) isotope records indicate that the oxygen minimum zone (OMZ) expanded laterally and to shallower depths (Algeo et al., 2010; Algeo et al., 2011; Lau et al., 2016; Meyer et al., 2011), potentially affecting organic carbon burial and authigenic carbonate precipitation. Thus, δ^{13}C in the Early Triassic may have fluctuated dramatically from changing organic carbon burial fluxes and associated Ω fluctuations—changes that should also be reflected in the $\delta^{44/40}$Ca record.

Although $\delta^{44/40}$Ca data have been collected in carbonate rocks for the ~0.5 Myr immediately bracketing the end-Permian mass extinction, such records have not yet been compiled for the subsequent 15 Myr. If δ^{13}C excursions in the Early Triassic are associated with changes in seawater carbonate chemistry, the related fluctuations in seawater Ca should result in $\delta^{44/40}$Ca excursions recorded in multiple contemporaneous stratigraphic records. If the observed records do not agree among sites, then other processes must be influencing $\delta^{44/40}$Ca in these carbonate rocks.

2. MATERIALS AND METHODS

2.1 Geologic Setting

In this study, we analyzed $\delta^{44/40}$Ca in samples from shallow-marine carbonate stratigraphic sections located in south China and Turkey. We focus on these localities because they are promising for capturing secular trends in Early to Middle Triassic seawater $\delta^{44/40}$Ca as C and U isotopic data show general agreement between sections (Lau et al., 2016).

2.1.1 Dajiang section, Great Bank of Guizhou, south China

The Great Bank of Guizhou (GBG) is an exceptionally preserved isolated carbonate platform in the Nanpanjiang Basin of the equatorial eastern Tethys (Figure 1; Lehrmann et al., 1998). The platform is exposed in geologic cross-section along a syncline running roughly north to south at the town of Bianyang (Lehrmann et al., 1998). Previous studies of the GBG have established a stratigraphic framework, including the platform architecture and sedimentology (Lehrmann et al., 2001; Lehrmann et al., 2005; Lehrmann et al., 1998; Li et al., 2012; Minzoni et al., 2013) and age constraints from biostratigraphy, geochronology, and δ^{13}C chemostratigraphy (Krull et al., 2004; Lehrmann et al., 2006; Lehrmann et al., 2015). Paleontological studies in the GBG have been critical for determining the nature and timing of the biotic recovery from the end-Permian mass extinction (Chen et al., 2013; Payne et al., 2006a; Payne et al., 2006b; Payne et al., 2011; Song et al., 2011; Song et al., 2012b). In addition, numerous geochemical studies on environmental conditions during the extinction have been conducted at the GBG (Algeo et al., 2013; Brennecka et al., 2011; Lau et al., 2016; Meyer et al., 2011; Payne et al., 2010; Song et al., 2013; Song et al., 2014; Song et al., 2012a; Sun et al., 2012).

Exceptional exposure of the platform permits measurement of stratigraphic sections and collection of high-resolution sample sets recording the full interval from platform initiation during the latest Permian to drowning and termination during the Late Triassic (Figures 1, 2). At Dajiang (N25°33’59”, E106°39’36”), a 2500 m-thick shallow-marine section (intertidal to tens of meters water depth) in the platform interior, the uppermost Permian fossiliferous limestone is overlain by 8 to 16 m of thrombolitic microbialite at the Permian/Triassic transition (Lehrmann et al., 2003). Lower Triassic strata continue with ~50 m of thin-bedded lime mudstone and ~100 m of overlying oolitic dolo-grainstone. The Induan-Olenekian boundary is located at the start of ~180 m of peritidal cyclic limestone, which is overlain by ~700 m of pervasively dolomitized peritidal facies containing the Lower-Middle Triassic boundary (Lehrmann et al., 2001). During the Middle and Late Triassic, the GBG accumulated vertically, forming high-relief escarpments along the platform margin. Possibly rimmed by reefs that later collapsed along the platform margin, the platform resembled an atoll with a lagoon in the platform interior. Strata consist of 600 m of bioturbated molluscan-peloidal wackestones and packstones with occasional oncolites and domal stromatolites. These wackestones and packstones are overlain by 400 m of shallowing-upward fossiliferous peritidal cycles, after the platform returned to a flat-topped profile. Near the top of the Middle Triassic, strata consist of skeletal-peloidal packstones that were deposited in subtidal environments. Carbonate deposition was terminated by drowning of the platform and a higher influx from siliciclastic sediments in the Carnian substage of the Late Triassic (Lehrmann et al., 1998; Lehrmann et al., 2007).

In this study, we analyzed a suite of 45 new samples for $\delta^{44/40}$Ca from the Dajiang section. Combined with data previously published by Payne et al. (2010), the Ca isotopic record for Dajiang includes data from 69 samples (refer to Table 1 for details).

2.1.2 Taşkent, Turkey

To determine whether variations in $\delta^{44/40}$Ca are globally reproducible, we also analyzed limestone samples from the Aladag Nappe, Turkey. This region was located along the western Tethys (Figure 1), and is an allochthonous block that was thrust over the autochthonous series of the Tauride block during the Eocene (Altiner and Özgül, 2001; Monod, 1977; Özgül, 1997). The strata at Taşkent (N36°51', E32°30') contain a ~1000 m-thick shallow-marine mixed carbonate and siliciclastic section that spans the Upper Permian to the Middle Triassic (Figure 3; Groves et al., 2005; Richoz, 2006). The measured section begins with 48 m of uppermost Permian fossiliferous lime packstone. The Permian/Triassic boundary is contained within a 0.5 m bed of oolitic limestone overlain by 1 m of microbialite. Lowermost Triassic strata include 20 m of lime mudstone overlain by 25 m of oolitic grainstone. The next ~600 m, which contain the remainder of Lower Triassic stratigraphy and the Lower/Middle Triassic boundary, consist of alternating beds of 10 cm- to 5 m-thick strata of fine-grained limestone, 0.5 to 2 m-thick strata of oolitic packstone and grainstone, and <1 m- to 6-m thick strata of shale. Middle Triassic stratigraphy continues with 11 m of massive lime wackestone-packstone, overlain by 132 m of covered shale.

Alternating massive lime packstone (strata of 3 m to 27 m thickness, with some oolitic beds) and covered shale (strata of 1 m to 9 m thickness) continue for the remainder of the section.

The $\delta^{44/40}$Ca record from Taşkent comprises 60 samples. The geochronologic, lithostratigraphic, and biostratigraphic framework for Dajiang and the GBG has been well studied (Lehrmann et al., 2006; Lehrmann et al., 2015; Meyer et al., 2011), whereas the biostratigraphic and geochronologic constraints at Taşkent are less detailed (Altiner and Özgül, 2001; Monod, 1977; Özgül, 1997). We correlate Dajiang and Taşkent using a combination of geochronology, conodont and foraminiferan biostratigraphy, and δ^{13}C chemostratigraphy (Lau et al., 2016).

2.2 Analytical Methods

Carbon and oxygen (O) isotope data and some elemental concentration data from Dajiang were previously published by Payne et al. (2004) and (2010) and Meyer et al. (2011). Carbon and O isotope data and some elemental concentration data for Taşkent samples were previously published by Lau et al. (2016). Additional trace metal concentrations were obtained from powders dissolved with 1 N acetic acid and analyzed on an Inductively Coupled Plasma-Optical Emission Spectrometer (ICP-OES) at Stanford University. Reproducibility was better than ±5% (2SD).

Twenty-eight samples from Dajiang and 20 samples from Taşkent were analyzed for $\delta^{44/40}$Ca at the Center of Isotope Geochemistry (CIG) at the University of California, Berkeley. A 0.8 mm dental drill bit was used to produce at least 1 mg of carbonate powder per sample, targeting micrite and avoiding areas of alteration, such as veins. After adding 1 mL of 1 N acetic acid to the powder in a 1.5 mL centrifuge tube, the sample was digested overnight. After centrifuging to separate the undigested residue, 0.5 mL of the supernatant was removed and dried down in a Savillex^{TM} beaker. The sample was re-dissolved in 3 N nitric acid (HNO_3). An aliquot (equivalent to 30 μg of Ca) was decanted and 280 μL of Ca double spike was added. The spiked samples contained approximately 3 μg of ^{42}Ca and ^{48}Ca and yielded a final ^{42}Ca/^{44}Ca ratio of ~2.5. After drying down to completion, the sample was re-dissolved in 3 N HNO_3, and Ca was separated from Sr and other matrix elements using ~100 mL of element-specific DGA Eichrom Technologies resin. Purified samples were dried down and re-dissolved in 3 N HNO_3. Approximately 3 μg of Ca was loaded onto a zone-refined Re filament (as part of a double filament assembly), treated with 3 N H_3PO_4, and analyzed using a Thermo-Fisher Triton multi-collector thermal ionization mass spectrometer (TIMS) in the CIG following methods described in Fantle and Higgins (2014). At least two aliquots per sample were analyzed. Calcium isotope values are reported relative to Bulk Silicate Earth (BSE) ($^{40}Ca/^{44}Ca = 47.162$ and $^{42}Ca/^{44}Ca = 0.31221$), which has a value of -0.9‰ relative to modern seawater and 1‰ relative to SRM-915a (Fantle and Tipper, 2014). Replicates of SRM-915a had a mean $\delta^{44/40}$Ca of -1.06 ± 0.15‰ (2SD), within the expected range.

The remaining 17 samples from Dajiang and 40 from Taşkent were analyzed at GEOMAR, Helmholtz Centre for Ocean Research Kiel, following methods described in Griffith et al. (2008) and Heuser et al. (2002). Sample powders produced as described above were dissolved in 2.5 M hydrochloric acid (HCl). Following digestion, a $^{43}Ca/^{48}Ca$ double spike was added (Heuser et al., 2002). After drying down to completion, the sample was re-dissolved in 2.5 N hydrochloric acid (HCl) for separation using pre-washed cation exchange resin (BioRad AG50W). Purified samples were dried down and re-dissolved in 2.5 N HCl and loaded with a Ta_2O_5 activator on zone-refined Re single filaments in a double filament assembly. Calcium isotope analyses were performed on a Triton TIMS at GEOMAR following methods described in Heuser et al. (2002). Three aliquots per sample were analyzed and $\delta^{44/40}$Ca values are reported relative to BSE. An in-house CaF_2 standard was analyzed with each run and produced a mean of 0.14 ± 0.1‰. External precision is calculated as 2 standard deviations (2σ) from repeat measurements of the same sample solution, and has a mean of 0.1‰.

3. RESULTS

3.1 Dajiang, GBG, south China

Combined with previously published data, the Dajiang $\delta^{44/40}$Ca data exhibit three major features (Figure 2). First, as described in Payne et al. (2010), there is a negative 0.4‰ excursion at the Permian/Triassic boundary, where $\delta^{44/40}$Ca values decrease from ~-0.3‰ to -0.7‰. From 90 m to 220 m, $\delta^{44/40}$Ca values gradually return to baseline values. Second, $\delta^{44/40}$Ca decreases by 0.3‰ and reaches a minimum of -0.5‰ at ~350 m. This negative excursion, which has not previously been reported, is followed by a recovery to baseline values at ~500 m, and $\delta^{44/40}$Ca values remain near the pre-extinction baseline until the Lower/Middle Triassic boundary. Third, $\delta^{44/40}$Ca values hover around a mean of ~0.1‰ for the remainder of the 2000 m of stratigraphic section. Seventeen dolomitized samples fall in the stratigraphic range of 120 m to 180 m and 400 m to 1000 m, and have $\delta^{44/40}$Ca values that are slightly but not significantly more positive than nearby limestone samples. A t-test comparison of overlapping limestone and dolomite $\delta^{44/40}$Ca data from the Smithian substage produces a mean difference of 0.2‰ and a *p*-value of 0.05.

3.2 Taşkent, Turkey

At Taşkent, $\delta^{44/40}$Ca values exhibit a negative shift of -0.5‰ at the extinction horizon and reach a minimum of -1.1‰, followed by a steady positive trend, reaching a maximum of -0.1‰ at a stratigraphic height of ~200 m (Figure 3). At ~300 m, $\delta^{44/40}$Ca values again decrease to values of -0.9‰. Calcium isotope values then increase to -0.5‰ at ~400 m and remain relatively steady to the end of the measured stratigraphic section. There are only three dolomitized samples at Taşkent.

3.3 Combined records

To facilitate comparison between the stratigraphic sections, we produced smoothing curves for the Dajiang and Taşkent data sets (*smooth.spline* function in R). To capture the analytical uncertainty, we assume a Gaussian distribution defined by the 2σ of each data point and used a Monte Carlo routine to resample 200 times within these bounds (Fantle, 2010). The datasets overlap during the Changhsingian, Induan and Olenekian stages (Figure 4). Due to dolomitization of upper Smithian and Spathian (substages of the Olenekian) strata at Dajiang, only data from Taşkent are available for this interval. Accordingly, there is limited Middle-Upper Triassic overlap between these two sections. At the Permian/Triassic boundary, the $\delta^{44/40}$Ca data show similar trends and decrease in uppermost Permian strata followed by a return in Induan strata, although the absolute values are offset by ~0.3 to 0.4‰. Within the Dienerian strata, the records diverge. At Dajiang, $\delta^{44/40}$Ca values exhibit a short-lived negative excursion of 0.3‰, whereas $\delta^{44/40}$Ca values at Taşkent are similar to the pre-extinction values of that section. In the mid-Smithian, $\delta^{44/40}$Ca at Taşkent shifts to more negative values and remains at -0.5‰ for the remainder of the section, through the Anisian interval. In contrast, $\delta^{44/40}$Ca at Dajiang in the Smithian through the Middle Triassic varies between -0.2 and 0.1‰, and is positively offset by 0.3 to 0.6‰ from Taşkent.

3.4 Geochemical indicators of alteration

To determine the influence of dolomitzation and/or diagenetic alteration on the $\delta^{44/40}$Ca records at Dajiang and Taşkent, we measured or compiled δ^{18}O, Mg/Ca, Mn/Sr, [Sr], and [Mn]

(Figure 5). Dolomitization increases the Mg/Ca ratios of carbonates, and δ^{18}O and Mn/Sr ratios are useful indicators of diagenetic alteration by anoxic, Mn-enriched brines or ^{18}O- and Sr-depleted meteoritic fluids (Brand and Veizer, 1980). Because our sites were located at opposite margins of the Tethys Ocean, the post-depositional alteration regimes experienced by these sediments likely differed. At Taşkent, Induan δ^{18}O values have a mean of -7 ± 2‰ (n=60; all confidence intervals reported as 2SD), whereas mean δ^{18}O in contemporaneous samples at Dajiang is -4 ± 2‰ (n=71). In contrast, Mn/Sr ratios remain low for both sections, except for dolomitized samples and Griesbachian thrombolitic or oolitic samples. The [Sr] and [Mn] are higher at Taşkent than at Dajiang. At Dajiang, [Sr] range from 34 to 1463 mg/kg, with a mean of 351 mg/kg (n=71), whereas at Taşkent, [Sr] range from 99 to 3779 mg/kg, with a mean of 1059 mg/kg (n=60). The [Mn] at Dajiang have a mean of 87 mg/kg (n=71) and range from 2 to 1019 mg/kg, and [Mn] at Taşkent have a mean of 144 mg/kg (n=60) and range from 11 to 804 mg/kg.

To check for variation in $\delta^{44/40}$Ca that could be explained entirely by alteration, we assessed the correlation of $\delta^{44/40}$Ca with δ^{18}O, δ^{13}C, Mg/Ca, Mn/Sr, [Sr], and [Mn] (Figure 6; Table 2). The scatter plot of $\delta^{44/40}$Ca versus δ^{18}O highlights a major difference between the two sections: the Taşkent carbonates have lower $\delta^{44/40}$Ca with δ^{18}O values than the Dajiang carbonates, with little overlap between these two sections. Correlations of $\delta^{44/40}$Ca with δ^{18}O and [Mn] (Table 2) are significant at Dajiang (n=69; Spearman's ρ=0.34, *p*-value <0.01 and ρ=-0.31, *p*-value=0.01, respectively) but are not statistically significant at Taşkent (n=60; ρ=-0.13, *p*-value=0.31 and ρ=0.19, *p*-value=0.15, respectively) (Table 2). However, the directions of these correlations are opposite to the predicted positive and negative correlations of $\delta^{44/40}$Ca with δ^{18}O and [Mn], respectively, assuming $\delta^{44/40}$Ca trends to more positive values during diagenetic alteration at equilibrium with seawater (Fantle and DePaolo, 2007) and greater depletion of ^{18}O and enrichment of Mn from diagenetic interaction with anoxic fluids. At Taşkent, correlation between $\delta^{44/40}$Ca and Mn/Sr, as a measure of exchange with Mn-enriched and Sr-depleted fluids (Brand and Veizer, 1980), is significant (n=60, ρ=0.28, *p*-value=0.03). However, Mn/Sr values are well below 1.0, and thus are inconsistent with a high degree of alteration (Kaufman et al., 1993). There is no significant correlation between $\delta^{44/40}$Ca and Mn/Sr for Dajiang. Finally, $\delta^{44/40}$Ca for both Dajiang and Taşkent exhibits significant negative correlations with [Sr]. Although carbonate [Sr] can be modulated by diagenesis, it is subject to additional controls as discussed in detail below in *4. Discussion*.

The fabric of a carbonate rock affects the extent of diagenetic alteration because grain size is roughly correlated with surface area, which affects the rate of dissolution. Specifically, larger grain sizes generally have slower rates of dissolution (Walter and Morse, 1984), and thus may limit diagenetic alteration. Matrix-supported limestones, which are dominated by smaller grain sizes (*i.e.*, mudstones, wackestones), have greater porosity but lower permeability than grain-supported ones (*i.e.*, grainstones and packstones), decreasing the ratio of water-to-rock exchanged (Enos and Sawatsky, 1981). The dolomitized samples (Figure 6) from both sections have more positive δ^{18}O and $\delta^{44/40}$Ca compositions than limestones. Along with thrombolitic (microbialite) samples, samples that are dolomitized or grain-supported also have high Mn/Sr ratios, with dolostones having especially low [Sr] and thrombolites having high [Mn]. Mudstones and wackestones have lower δ^{18}O compositions and thus may be more altered. Oolites have high δ^{13}C values at Dajiang. At Taşkent, oolites have more negative $\delta^{44/40}$Ca compositions. Other than relatively positive $\delta^{44/40}$Ca values, packstones and grainstones do not differ from mudstones/wackestones in these geochemical indices of diagenesis.

4. DISCUSSION

The $\delta^{44/40}$Ca records from Dajiang, south China, and Taşkent, Turkey, differ in both their temporal trends and their absolute values. Although the negative excursion of ~0.3‰ at the end-Permian mass extinction at Dajiang (Payne et al., 2010) occurs also at Taşkent, the Taşkent $\delta^{44/40}$Ca values are almost 0.4‰ more negative than those at Dajiang. A similar trend in $\delta^{44/40}$Ca occurs in hydroxyapatite conodont elements collected from Meishan, south China (Hinojosa et al., 2012). Thus, the $\delta^{44/40}$Ca trends appear to record secular changes in the global Ca cycle, but the observed offset suggests that local effects have shifted absolute values. Through the remainder of the Early and Middle Triassic, there is little evidence for large excursions. The Dajiang record contains a second negative excursion of slightly smaller magnitude at ~251.4 Ma, which is not observed at Taşkent. Instead, $\delta^{44/40}$Ca values at Taşkent shift towards more negative values at 251.1 Ma but do not return to pre-extinction values and remain consistently more negative than those from Dajiang, with an offset ranging from 0.3 to 0.6‰.

The use of carbonate $\delta^{44/40}$Ca data to infer trends in seawater composition assumes that the fractionation factor between seawater and carbonate can be inferred, and that Ca is derived from seawater. However, the degree to which our $\delta^{44/40}$Ca data have been overprinted by local, syn-depositional or post-depositional factors needs to be considered. We use the relationship between the $\delta^{44/40}$Ca and [Sr] to distinguish between these factors. From this framework, we propose a model that combines isotopic and elemental change during recrystallization with differences in initial carbonate mineralogy to explain the observed trends.

4.1 Post-depositional processes and potential impact on $\delta^{44/40}$Ca in carbonate rocks

The original depositional $\delta^{44/40}$Ca of bulk carbonates can be altered via various local syn-depositional and post-depositional processes such that it no longer tracks seawater $\delta^{44/40}$Ca (*e.g.*, Fantle and Higgins, 2014; Fantle, 2015; Farkaš et al., 2016; Griffith et al., 2015; Husson et al., 2015; Jost et al., 2014 and 2017). Bulk geochemical composition can be diagenetically altered from precipitation of authigenic carbonate (cementation and reduction in porosity) or via recrystallization (dissolution and replacement with no change in porosity). Diagenetic processes are further differentiated by the source of fluids exchanging with the carbonate rock. Unlike the original depositional $\delta^{44/40}$Ca value, which is offset from seawater by ~-1 to ~-1.7‰ depending on the polymorph of $CaCO_3$ that precipitates (*e.g.*, Gussone et al., 2005), the $\delta^{44/40}$Ca value of carbonates precipitated during recrystallization (including authigenic cements) reflects isotopic equilibrium with porewater Ca, with little to no fractionation (DePaolo, 2011; Fantle and DePaolo, 2007; Fantle, 2015). Thus, the porewater source and its associated $\delta^{44/40}$Ca influence the alteration of $\delta^{44/40}$Ca in carbonate rock.

For example, early marine diagenesis occurs within the upper sediment column (in which sediments are not yet well cemented), where the Ca in carbonate sediments exchanges with porewater in communication with seawater (*e.g.*, Berner 1980). Early diagenetic processes such as dissolution of biogenic carbonates, ion exchange due to ammonium production, and organic carbon remineralization may all result in porewater $\delta^{44/40}$Ca values that are more negative than seawater by 0.6 to 0.8‰ (Teichert et al., 2009). Subsequent authigenic $CaCO_3$ precipitation or recrystallization at equilibrium—with little to no fractionation (DePaolo 2011; Fantle and DePaolo, 2007; Fantle, 2015)—would result in a minor to negligible positive offset. Although models of early marine diagenesis assume bottom waters diffuse into the sediments, advection of seawater (in some cases on continental shelves mixed with groundwater) can be driven by gradients in hydraulic head, density, and temperature (Whitaker and Smart, 1990). Exchange with hydrothermal or burial diagenetic fluids (often reducing brines) occurs at depth in the sediment column and often >10^6 years after initial deposition (*e.g.*, Moore, 1989). Meteoric diagenesis is primarily driven by advection and can occur either during early diagenesis or much later if the strata are subsequently uplifted. Although subaerial exposure occurred periodically at Dajiang and Taşkent during deposition of the strata, we do not observe correlations between $\delta^{44/40}$Ca and sequence boundaries (indicative of subaerial erosion surfaces; Figures 2 and 3).

In addition to interaction with fluids, the carbonate minerals themselves can undergo localized structural changes that alter their geochemical and isotopic compositions. Although "neomorphism" has been used broadly to refer to a change from an initial meta-stable carbonate phase to stable low-magnesian calcite (LMC), in this paper we define this process as the closed-system, solid-state transition of primary aragonite and high-magnesian calcite (HMC) to LMC in the absence of exchange with porewaters (Machel, 1997). In contrast, we use "recrystallization" to mean the dissolution and re-precipitation of carbonate minerals (that may include but does not require a change in mineralogy) and can result in geochemical exchange with porewaters (Machel, 1997). Finally, the timing of dolomitization and its fluid source remain challenging to infer, but numerous models indicate that both seawater and external fluids can be involved in this process (*e.g.*, Land, 1985).

4.2 Relationship between $\delta^{44/40}$Ca and [Sr]

4.2.1 Conceptual models

Numerous factors can affect carbonate $\delta^{44/40}$Ca values and the extent to which they reflect changes in seawater $\delta^{44/40}$Ca (summarized in Table 3). In addition to diagenetic alteration as described in the previous section, the original depositional $\delta^{44/40}$Ca value depends on $CaCO_3$ mineralogy and the net kinetic fractionation factor. To determine the relative importance of these factors, we focus on the observed relationship between $\delta^{44/40}$Ca and [Sr]. Strontium concentrations in carbonates can vary as a function of the size of the seawater Sr reservoir, which is controlled by the mass balance between continental weathering, hydrothermal circulation, and carbonate deposition (Goddéris and François 1995; Kump 1989; Steuber and Veizer, 2002). Assuming a constant offset between carbonate and seawater $\delta^{44/40}$Ca, an invariant distribution coefficient for Sr incorporation for each $CaCO_3$ polymorph, and a constant aragonite-to-calcite ratio, secular variations in both the Ca and Sr seawater cycles should be reflected in the carbonate rock record (Figure 7A).

Controls on the Ca kinetic fractionation factor between seawater and $CaCO_3$ (such as precipitation rate) can also affect [Sr], producing an apparent inverse, linear relationship between carbonate $\delta^{44/40}$Ca and [Sr] (*e.g.*, Tang et al., 2008a and 2008b; Watkins et al., 2017; Figure 7B). At equilibrium, Ca isotopes are not appreciably fractionated between $CaCO_3$ and aqueous Ca (*i.e.*, $\Delta_{c\text{-}s} = \sim 0‰$) (Fantle and DePaolo, 2007; Jacobson and Holmden, 2008), implying that fractionation arises from kinetic isotope effects and the relative rates of forward and backward reactions (DePaolo, 2011; Tang et al., 2008a). This equilibrium fractionation factor was derived from observations from deep-sea carbonate samples with estimated precipitation rates of $<10^{-17}$ mol/m^2/s (Fantle and DePaolo, 2007). In contrast, inorganic calcite precipitated in the laboratory at faster rates (between 10^{-8} and 10^{-5} mol/m^2/s) is modeled to exhibit a small equilibrium fractionation of -0.5 to -0.2‰ (DePaolo, 2011). Thus, theoretical considerations and experimental evidence suggests that as precipitation rate increases, $\Delta_{c\text{-}s}$ also increases (*e.g.*, Tang et al., 2008a; Watkins et al., 2017). We note that an inverse relationship between $\Delta_{c\text{-}s}$ and precipitation rates has also been observed (Lemarchand et al., 2004; AlKhatib and Eisenhauer, 2017a) suggesting that very minor perturbations in $\delta^{44/40}$Ca arise from an acidification event (Komar and Zeebe, 2016). Given the uncertainties in the relationship between the precipitation rate and $\Delta_{c\text{-}s}$, we use the Tang et al. (2008a) relationship because their experimental methods minimized transport limitations which complicate the relationship between rate and $\Delta_{c\text{-}s}$ (DePaolo, 2011). More impurities, such as Sr, are incorporated at higher precipitation rates (*e.g.*, Tang et al., 2008b; DePaolo, 2011), although in the presence of fluids with high Sr/Ca, calcite precipitation is inhibited by strain within the local crystal lattice and increasing mineral solubility (Nielsen et al., 2013). If porewater Sr/Ca remains constant (as would be the case for fluids derived from seawater), both the magnitude of $\Delta_{c\text{-}s}$ and degree of Sr incorporation in carbonates (K_{Sr}) increase as precipitation rate increases, producing a linear and inverse trend between [Sr] or Sr/Ca and $\delta^{44/40}$Ca (Figure 7B; Farkaš et al., 2007 and 2016; Steuber and Buhl, 2006; Tang et al., 2008a and 2008b; Watkins et al., 2017). This correlation is also predicted by modeling of inorganic calcite precipitation, where both $\Delta_{c\text{-}s}$ and K_{Sr} are described as functions of precipitation and dissolution rates (DePaolo, 2011; Watkins et al., 2017).

Carbonate $\delta^{44/40}$Ca and [Sr] also vary as a function of the $CaCO_3$ polymorph that is initially precipitated, with aragonite and LMC as end-members. Because aragonite has a larger cation site in its crystal lattice than calcite, aragonite is associated with higher [Sr] (*e.g.*, Kinsman, 1969). Additionally, precipitation of aragonite results in a larger Ca isotope fractionation from seawater, producing $\delta^{44/40}$Ca values that are more negative than calcite (Gussone et al., 2005; Blättler et al., 2012). Thus, variable mixtures of polymorphs could result in an inverse correlation between $\delta^{44/40}$Ca and [Sr] (Figure 7C; Farkaš et al., 2017). Although the initial aragonite-to-calcite ratio is unknown because metastable aragonite and HMC transform into LMC during neomorphism, this factor has been gaining favor as an explanation for $\delta^{44/40}$Ca trends across the Shuram δ^{13}C anomaly (Husson et al., 2015), the Hirnantian glaciation (Kimmig and Holmden, 2017), the end-Triassic mass extinction (Jost et al., 2017), and the Phanerozoic (Blättler et al., 2012). Secular variation in the aragonite-to-calcite ratio in global carbonate sediment has also been invoked to explain Phanerozoic $\delta^{44/40}$Ca seawater trends recorded in well-preserved biogenic calcite from brachiopods, belemnites, and foraminifera (Farkaš et al., 2007).

Interaction with submarine groundwater, which generally has low [Sr], would result in diagnostic patterns in $\delta^{44/40}$Ca and [Sr] (orange arrow in Figure 7D; Holmden et al., 2012b). Submarine groundwater discharge from local restriction is hypothesized to have decreased the $\delta^{44/40}$Ca composition and [Sr] of Hirnantian carbonate rocks relative to global seawater, resulting in a positive relationship between $\delta^{44/40}$Ca and [Sr] (Holmden et al., 2012a), although an updated interpretion attributes this relationship to changes in the variations in aragonite precipitation (Kimmig and Holmden, 2017). The effect of burial diagenesis on $\delta^{44/40}$Ca in bulk carbonate rock remains challenging to constrain as the effects of marine-derived fluids on carbonate $\delta^{44/40}$Ca are not well known. Interaction with Sr-rich hydrothermal fluids is predicted to produce an inverse relationship between $\delta^{44/40}$Ca and [Sr] (Figure 7D, purple arrow). The $\delta^{44/40}$Ca of hydrothermal fluids from the Mid-Atlantic Ridge and East Pacific Rise have $\delta^{44/40}$Ca values ~0.95‰ lighter than modern seawater (Amini et al., 2008; Schmitt et al., 2003), which could result in a small positive shift during recrystallization at isotopic equilibrium (assumed to be near unity; Brown et al., 2013). Similarly, deep porewaters (> 245 to 300 meters below seafloor) in interaction with oceanic basement are depleted in ^{44}Ca relative to seawater (Teichert et al., 2009). In contrast, early diagenetic recrystallization in the presence of seawater—assuming an equilibrium Δ_{c-s} of 0‰ (Fantle, 2015; Fantle and Higgins, 2014)—would instead result in a positive shift from the original composition (Figure 7D, gray arrow).

4.2.2 Comparison with Early-Middle Triassic $\delta^{44/40}$Ca and [Sr] data

Given the numerous factors that can potentially influence Ca and Sr in carbonate rocks and their predicted relationships between $\delta^{44/40}$Ca and [Sr], our records, along with literature data, provide a means to examine the dominant controls on the $\delta^{44/40}$Ca composition of carbonate rock. Because the $\delta^{44/40}$Ca and [Sr] data from Dajiang and Taşkent do not co-vary (Figure 4), we eliminate a secular change in seawater Ca and Sr (Figure 7A) as the principal factor controlling the stratigraphic trends in these carbonate rocks. Although our data roughly exhibit an inverse linear trend, we also consider a log-linear model where [Sr] is plotted on a logarithmic axis (Figure 8). We use standardized major axis (SMA) regression models (*sma* function in R) to evaluate the quality of fit between the linear and log-linear models. Unlike more common least-squares linear regression models, which assume one variable is the control and is known (usually plotted along the x-axis), SMA models assume that neither variable is the control and that both have measurement error. Using SMA, the inverse relationship between $\delta^{44/40}$Ca and [Sr] (Figure 8), is better described by a log-linear model (Spearman's ρ=-0.71, *p*-value<0.001) than a linear model. Using the Aikake information criterion (AIC) to evaluate the quality of the regression, the AIC for the log-linear fit is much lower than that for the linear fit (ΔAIC=-1902) and further supports a non-linear relationship. In contrast to the linear regression results, the log-linear SMA models are nearly identical when performed for each section and suggest common controlling factors (Figure 8). In fact, a single, common SMA model for the entire dataset produces a better fit (ΔAIC=-81) than separate models for the two sections. The preference for a log-linear model suggests that a non-linear process is producing Sr loss concurrently with an increase in $\delta^{44/40}$Ca.

The observed log-linear model relationship eliminates precipitation rate as a primary control on our dataset because a linear relationship is both predicted and observed between K_{Sr} and $\Delta_{c\text{-}s}$ when precipitation rate is the controlling variable (Figure 7B; DePaolo, 2011; Nielsen et al., 2012; Tang et al., 2008a and 2008b; Watkins et al., 2017). Because $CaCO_3$ saturation state fluctuated during this time interval (Baud et al., 2007; Pruss et al., 2006; Weidlich and Bernecker, 2001; Woods et al., 2009), changes in fractionation from variations in precipitation rate probably occurred. However, the lack of a clear linear relationship (*e.g.*, Farkaš et al., 2016) suggests that this was not the major factor in determining the [Sr] and $\delta^{44/40}$Ca in our carbonate rocks. Mixing between aragonite and calcite end-members results in a linear relationship between [Sr] and $\delta^{44/40}$Ca (Figure 7C); our observation of a log-linear relationship for [Sr] with $\delta^{44/40}$Ca suggests that local variation in the relative proportions of $CaCO_3$ end-members can only partially explain the dataset. Open-system alteration under the influence of external sources such as groundwater and burial fluids (Figure 7D) as principal controls on our data is also inconsistent with our data because we observe neither a positive correlation nor an enrichment in Sr, respectively. Furthermore, our statistical results (*section 3.4*) comparing $\delta^{44/40}$Ca to diagenetic indicators show that although we did find significant correlations of $\delta^{44/40}$Ca with δ^{18}O, [Mn], and Mn/Sr, the direction of the correlation (Figure 6) is generally opposite to the expected relationship under meteoric or burial diagenesis, or the influence of groundwater and local restriction. Thus, diagenetic resetting with meteoric or reducing fluids is unlikely to fully account for the trends in $\delta^{44/40}$Ca. Similarly, the absence of correlation between Mg/Ca and $\delta^{44/40}$Ca argues against dolomitization as a primary control on the $\delta^{44/40}$Ca composition. Instead, we suggest that variation in initial carbonate mineralogy through time and between stratigraphic sections (Figure 7C), combined with alteration and exchange with porewater in communication with seawater, best account for the offset between the sections (Figure 7D, gray arrow).

4.2.3 Insights from a water-rock interaction model of exchange with seawater

Because of the observed log-linear relationship between $\delta^{44/40}$Ca and [Sr] (Figure 8), our data cannot be fully explained by variations in the initial aragonite-to-calcite composition. However, early diagenetic recrystallization superimposed on samples with differing initial aragonite-to-calcite ratios can account for the pattern. An open-system water-rock interaction model (based on Banner and Hanson, 1990; Figure 9, Table 4) shows that exchange with porewater in communication with seawater results in a redistribution of isotopes towards a new equilibrium (*e.g.*, Fantle and DePaolo, 2007) that matches our observations. This simple equilibrium reaction model tracks the evolution of carbonate geochemical compositions with increasing interaction with a seawater-derived fluid. In the model, we evaluate the evolution of carbonate [Sr] and $\delta^{44/40}$Ca (as well as δ^{13}C and δ^{18}O for context) as a function of *N*, or the cumulative water-to-rock ratio (by mass), under the assumption that recrystallization occurs at equilibrium and thus $\Delta_{c\text{-}s} = 0$ ‰ (Fantle and DePaolo, 2007). We also assume that the concentrations and isotopic compositions of the elements of interest in porewaters are constant. Because recrystallization occurs rapidly in the upper part of the sediment column (<30 m), this calculation illustrates the potential for the bulk carbonate $\delta^{44/40}$Ca and [Sr] values to vary from their initial compositions during equilibration with porewater (Fantle, 2010; Fantle, 2015). Initial concentrations in the fluid and rock, their isotopic compositions, and fractionation factors are shown in Figure 9A-D, and a summary of model equations and parameters is presented in the Appendix and Table 4.

As recrystallization in equilibrium with porewaters proceeds, loss of Sr occurs more quickly than resetting of $\delta^{44/40}$Ca, resulting in non-linear evolution in $\delta^{44/40}$Ca versus [Sr] space (Figure 9E, F). Under this scenario, the diagenetic trajectory of [Sr] and $\delta^{44/40}$Ca better matches the log-linear relationship than the other factors described earlier. Different initial aragonite-to-calcite ratios also influence the diagenetic trajectory by shifting the starting bulk composition. Importantly, initial linear correlation between [Sr] and $\delta^{44/40}$Ca produced by variation in precipitation rate alone (Figure 7B) would not provide a mixture of carbonate minerals with differing susceptibility to early diagenetic alteration.

The diagenetic resetting of [Sr] and $\delta^{44/40}$Ca implied by our model can be reconciled with observations of fluid flow in modern carbonate platforms (*e.g.*, Whitaker and Smart, 1990). For the water-rock ratios invoked by this model, an N of 1000 is equivalent to 1 L of water exchanged for every gram of rock. Although the exact values of N predicted in our model can vary depending on the parameterizations of the modeled system (*e.g.*, porosity; *cf.* Husson et al., 2015), the important observation is the point at which each geochemical component is altered relative to the others. Regardless of the uncertainty in N, the fluxes of water required are substantial, and would be typical of advective rather than diffusive fluxes of seawater into pores. The recrystallization suggested by the model likely occurred at relatively shallow depths: the primary ^{87}Sr/^{86}Sr marine signatures preserved in these rocks (Schaal, 2014) indicates interaction with seawater-derived early diagenetic fluids.. Seawater can be advected within shallow marine sediments through an array of processes. For example, density flows driven by evaporative salinity gradients along a carbonate platform can generate pore velocities compatible with the values of N predicted by our model (Whitaker and Smart, 1990). To illustrate, assuming an initial porosity of 0.4 and a rock density of 3 g/cm^3, a gram of carbonate sediment would contain ~0.2 mL of pore volume (PV). One liter of water exchange is equivalent to ~5000 PV. Because PV can be defined in terms of fluid residence time, T:

$$T = PV * L/V \qquad (1)$$

where V is the pore velocity and L is the reaction length scale ~0.69 cm/g of rock, pore velocities on the order of 10^{-1} to 10^{1} cm/yr estimated from model simulations of salinity-driven density flows (Jones et al., 2006; Kaufman, 1994; Simms, 1984) would produce porewater residence times of 1 to 100 years. Additionally, a density gradient within a carbonate platform can persist for 100 times the duration of a salinity-driven fluid refluxing through the sediment (*i.e.*, latent reflux; Jones et al., 2006). In comparison to these time scales that are reasonable for recrystallization, temperature-driven Kohout flows and mixing driven by freshwater can pump seawater at Darcy velocities of 0.3-1 and 5-20 m/yr, respectively (Simms, 1984), fluxes too rapid for carbonate precipitation at isotopic equilibrium. Although our proposed density-driven reflux flows are typically invoked in models for dolomitization, reactive transport modeling suggests that slower rates of dolomitization are generated when rates of reflux are also slow (Jones and Xiao, 2005). Thus, at slow advective velocities, chemical alteration may potentially occur absent dolomitization.

In summary, the mechanism that can best model the log-linear relationship between [Sr] and $\delta^{44/40}$Ca is early diagenetic resetting from a range of initial aragonite-to-calcite $CaCO_3$ compositions. This allows for a common seawater $\delta^{44/40}$Ca to be inferred at both stratigraphic sections. The first-order hydrologic constraints imposed by our simple diagenetic model are reasonable based on studies of fluid flow through modern carbonate platforms.

4.3 Comparison of $\delta^{44/40}$Ca records from Dajiang and Taşkent

Although carbon and uranium require greater volumes of fluid exchange to be fully reset than calcium (Figure 9B; Lau et al., 2017), the agreement between the U and C isotope records at Dajiang and Taşkent (Lau et al., 2016) implies that diagenesis has not resulted in complete geochemical alteration. Therefore, these samples may retain the long-term $\delta^{44/40}$Ca value of the carbonate rock. If secular variations in seawater $\delta^{44/40}$Ca are also preserved in these samples, then the temporal trends of the carbonate rock $\delta^{44/40}$Ca should agree between Dajiang and Taşkent. Though the $\delta^{44/40}$Ca values show temporally cohesive trends with discernable temporal patterns for individual sections, neither the pattern nor the absolute value match (Figure 4). A ~0.4‰ negative $\delta^{44/40}$Ca excursion at the Permian/Triassic boundary is observed at both sections, but the minimum $\delta^{44/40}$Ca value at Dajiang is -0.7‰ compared to -1‰ at Taşkent. Late Smithian to Carnian $\delta^{44/40}$Ca values at both sections are relatively stable, but $\delta^{44/40}$Ca values at Dajiang have a mean of 0.0‰ whereas $\delta^{44/40}$Ca at Taşkent have a mean of -0.5‰. Although there is some uncertainty in the correlation, the δ^{13}C chemostratigraphy takes advantage of the large and well-defined positive and negative δ^{13}C perturbations in the Early Triassic. The negative $\delta^{44/40}$Ca isotope shift at Dajiang corresponds to a positive δ^{13}C excursion (Figure 2), whereas the opposite is true for Taşkent (Figure 3). Thus, it is unlikely that the discrepancy between south China and Turkey is primarily a factor of the age model and/or correlation.

This variability in carbonate $\delta^{44/40}$Ca may be attributed to local environmental conditions, which would also influence the mode of carbonate precipitation and rock fabric type (*e.g.*, grain-supported, matrix-supported, microbialite). The ANOVA results indicate that the $\delta^{44/40}$Ca data are not significantly different when grouped by fabric type at Taşkent (Table 5). The opposite is observed at Dajiang, as ANOVA results indicate that $\delta^{44/40}$Ca is significantly associated with fabric type (p-value <0.001; Table 5, Figure 10). Because $\delta^{44/40}$Ca values in rocks with grain-supported fabrics are significantly more positive than those with matrix-supported fabrics, a plausible interpretation is that more permeable sediments at Dajiang experienced greater diagenetic resetting. Below, we further explore how variability in local depositional environments may explain the differences in the $\delta^{44/40}$Ca values of our two sections.

4.3.1 Local environmental variations

We propose that variations in the original aragonite-to-calcite mineralogy are the most plausible explanation for the isotopic differences between stratigraphic sections. If aragonite was the dominant original CaCO$_3$ polymorph at Taşkent whereas calcite was the dominant original polymorph at Dajiang, one would expect higher [Sr] and Sr/Ca and more negative $\delta^{44/40}$Ca at Taşkent, consistent with observations (Figure 8) and our recrystallization model (Figure 9). Additionally, the ~0.3 to 0.6‰ offset in $\delta^{44/40}$Ca between the two sections falls within the ~0.5‰ difference in fractionation factor between calcite and aragonite (Gussone et al., 2005) and, therefore, can be explained by systematic differences in their original admixtures of CaCO$_3$ polymorphs. In other words, seawater $\delta^{44/40}$Ca was the same during deposition (as expected), but the precipitated carbonate $\delta^{44/40}$Ca fell between an aragonite-dominated end-member with [Sr] ~3000 mg/kg and $\delta^{44/40}$Ca ~-1% and a calcite-dominated end-member with [Sr] ~400 mg/kg and $\delta^{44/40}$Ca ~0%. As noted in *section 4.2.2*, the combined data do not fall along the predicted linear mixing curve between aragonite and calcite end-members (Figure 9E). It would be expected that the linear regression lines for the two sections would overlap if the [Sr] and $\delta^{44/40}$Ca of the CaCO$_3$ end members were similar for the two stratigraphic sections; this is not the case. Although local carbonate mineralogy can only partially explain the relationship between $\delta^{44/40}$Ca and [Sr], it can explain the offset between the Dajiang and Taşkent data.

The Ca isotope fractionation during $CaCO_3$ precipitation varies with temperature (*e.g.*, AlKhatib and Eisenhauer, 2017a,b; Gussone et al., 2005; Marriott et al., 2004); however, fractionation is driven by kinetic effects and temperature is not the primary control (Brown et al., 2013; DePaolo, 2011; Nielsen et al., 2012). In any case, the difference in $\delta^{44/40}$Ca between stratigraphic sections is too large to be fully attributed to temperature differences. Given a positive relationship between $\Delta_{c\text{-}s}$ and temperature of ~0.02‰ per °C (Gussone et al., 2005; Marriott et al., 2004), the ~0.3 to 0.6‰ offset (Figure 4) implies that sea surface temperatures in Turkey were 15 to 25 °C colder than in South China. This range exceeds the variability in modern tropical sea surface temperatures. Additionally, an increase in temperature coincident with the end-Permian extinction horizon (Romano et al., 2013; Sun et al., 2012) would decrease precipitation rate and $\Delta_{c\text{-}s}$, predicting a positive excursion in the $\delta^{44/40}$Ca of the rocks—opposite of the observed pattern.

Calcium in groundwater can affect the $\delta^{44/40}$Ca in coastal sites (Holmden et al., 2012b). Both sections were situated in shallow-marine environments: Taşkent on an attached carbonate ramp, and Dajiang in the interior of an isolated carbonate platform. In both environments, freshwater—influenced by carbonate dissolution—may have mixed with seawater, resulting in carbonates precipitated with a more negative $\delta^{44/40}$Ca composition relative to seawater. This hypothesis is supported by the relatively negative δ^{18}O values at Taşkent, potentially caused by mixing with meteoric waters or resetting during recrystallization; but the high [Sr] at Taşkent does not support the influence of Sr-depleted groundwater (Brand and Veizer, 1980). Additionally, significant groundwater intrusion predicts large salinity gradients (Holmden et al., 2012b); in contrast, the faunas at Dajiang and Taşkent are representative of normal marine salinities (Payne et al., 2006b, 2007), indicating that the depositional environments of the studied stratigraphic sections experienced open marine circulation. Hence, it is unlikely that groundwater is the primary process contributing to the observed $\delta^{44/40}$Ca differences.

Remineralization of organic matter within the upper sediment column can result in the release of organically-bound ^{40}Ca into porewaters, driving bulk carbonate $\delta^{44/40}$Ca to more negative values (Teichert et al., 2009). It is unlikely that organic matter oxidation played an important role at our sites because total organic carbon (TOC) contents for limestone samples are generally very low, with a mean of 0.4% for Dajiang and 0.3% for Taşkent (Lau et al., 2016). Deep fluids that have reacted with ocean crust would also have low [Sr] and ^{87}Sr/^{86}Sr (Teichert et al., 2009), but our stratigraphic sections were deposited on continental crust and positive correlations with $\delta^{44/40}$Ca are not observed (Figure 6). Additionally, ^{87}Sr/^{86}Sr data from these sections are normal marine to slightly radiogenic (Schaal, 2014).

A biological control on the fractionation factor of Ca is also improbable. In this scenario, higher proportions of aragonitic sponges, molluscs, foraminifera, and echinoderms, which exert a strong biological control on the precipitation rate of $CaCO_3$, result in larger Δ_{c-s} than brachiopods, red algae, and calcitic sponges, which either precipitate calcite skeletons or demonstrate a weaker control on the precipitation rate (Blättler et al., 2012). The paucity of skeletal grains at both sections, where the approximate rock area comprising skeletal material is on average less than 4% (Table 6), and the $\delta^{44/40}$Ca values for samples with >10% skeletal components are indistinct from those with <10% (t-test p-value = 0.13). Thus, a change in vital effects is unlikely to be the primary control on $\delta^{44/40}$Ca.

4.3.2 Microfacies and petrographic observations

To investigate differences in original $CaCO_3$ mineralogy between Dajiang and Taşkent, we collected petrographic data from thin sections to identify the prevalence of primary (*e.g.*, micrite, skeletal), early diagenetic (*e.g.*, microcrystalline cement, recrystallized clasts), or burial diagenetic (*e.g.*, sparry calcite) microfacies. We examined thin sections from a subset of samples (27 from Dajiang and 10 from Taşkent) and visually estimated the area of the thin section composed of each microfacies type (Table 6).

This first-order analysis provides us with clear differences in sedimentation, porosity, and degree of recrystallization between stratigraphic sections and through time. In general, micritic facies comprose a larger proportion of microfacies at Dajiang, followed by microcrystalline cement. In fact, micrite composes a large proportion of almost all the examined thin sections from above the Permian/Triassic boundary, which is dominated by early diagenetic microcrystalline cements and burial diagenetic sparry calcite. The micrite directly above the boundary is distinct from micrite in other intervals because it is a component of the microbial framework of the boundary thrombolites (Payne et al., 2006b). Skeletal grains are limited at Dajiang above the end-Permian extinction horizon. Micrite is also an important component of Taşkent carbonates, but these rocks contain a larger proportion of grains—mostly recrystallized peloids, ooids, and other clasts—and are much more heterogeneous in composition among samples. At Taşkent, micrite is most dominant in strata bracketing the Permian/Triassic boundary, but is not a volumetrically important component for the rest of the section. Hand sample observations for intervals without associated thin sections also illustrate that ooids and peloids are common.

Differences in sedimentary fabrics may provide insight into the chemical differences between Dajiang and Taşkent. First, ooids and peloids are especially prevalent at Taşkent (Groves et al., 2005; Richoz, 2006) but are much more limited at Dajiang. Although we are unable to determine the original mineralogy of these clasts at Taşkent, giant ooids from the GBG were initially aragonitic or bimineralic (Lehrmann et al., 2012; Payne et al., 2006a). This observation is consistent with our hypothesis that aragonite-dominated $CaCO_3$ precipitation could have been a controlling factor on $\Delta_{c\text{-}s}$ and therefore differences in $\delta^{44/40}$Ca (*e.g.*, Kimmig and Holmden, 2017). Second, the greater proportion of grain-supported lithologies at Taşkent favor very early cementation of aragonite—also supported by high [Sr] that indicate precipitation from seawater-like fluids.

Dajiang $\delta^{44/40}$Ca values are comparable to modern inorganic calcite (Blättler et al., 2012). Petrographic observations and evidence for aragonitic seas (Stanley, 2006) indicate that inorganic calcite is unlikely to have precipitated in this section for the entire time interval. Therefore, these data could also be influenced by a reset of $\delta^{44/40}$Ca to more positive compositions during recrystallization. Tukey-Kramer statistical results (Table 5) are consistent with this hypothesis: $\delta^{44/40}$Ca values in matrix-supported samples are 0.29‰ more negative than grain-supported samples (Figure 10). Early diagenetic recrystallization has been invoked to explain a positive 0.15-0.8‰ shift in $\delta^{44/40}$Ca (Fantle and DePaolo, 2007; Griffith et al., 2015). The magnitude of this offset is predicted to increase with lower sedimentation rates because this would increase the residence time of the carbonate sediments at the depths at which porewater pH decreases from aerobic respiration, which can result in open-system diagenesis and a positive shift in $\delta^{44/40}$Ca (Griffith et al., 2015). However, the shallow-marine environment of our studied sections is characterized by high sedimentation rates. Despite occasional depositional hiatuses, we do not observe evidence for positive excursions associated with these events at either section. Therefore, it is most plausible that the generally more negative $\delta^{44/40}$Ca values at Taşkent are a function of original aragonite-to-calcite ratios, but some of the temporal variations are due to recrystallization, controlled by carbonate fabric type. Additionally, because changes in saturation state can produce variations in precipitation rate, the effect of saturation state on precipitation rate may also partially explain some of the variability in our $\delta^{44/40}$Ca data (*e.g.*, Silva-Tamayo, in review).

4.4 Other carbonate $\delta^{44/40}$Ca records

An inverse relationship between [Sr] and $\delta^{44/40}$Ca was previously observed for Ediacaran carbonates from Australia (Husson et al., 2015), Ordovician carbonates from the western United States (Holmden et al., 2012a), Upper Silurian carbonates from the Czech Republic (Farkaš et al., 2016), and Triassic/Jurassic carbonates from Italy (Jost et al., 2017). Similar to the model presented herein, Husson et al. (2015) propose that the log-linear relationship between [Sr] and $\delta^{44/40}$Ca in the Ediacaran Wonoka Formation spanning the Shuram negative δ^{13}C excursion falls within an array defined by mixing between calcite and aragonite end-members with various degrees of Sr loss. The combination of our data and model illustrates that although multiple sections do not exhibit the same absolute value of $\delta^{44/40}$Ca, this difference can be attributed to different mixtures of primary $CaCO_3$ polymorphs that fall along similar diagenetic trajectories.

To determine if a common mechanism explains both data reported herein and previously published observations from other localities spanning numerous geological periods, we compiled previously published $\delta^{44/40}$Ca data measured in shallow-marine carbonate rocks that also evaluated Sr concentrations or ratios (Figure 11). In addition to the studies mentioned above, these include Ediacaran carbonates from China (Sawaki et al., 2014), Ordovician carbonates from Canada (Holmden, 2009), Permian carbonates from Turkey and China (Jost et al., 2014), and Permian/Triassic carbonates from Oman and Italy (Silva-Tamayo, in review). Core-top sediments deposited in shallow waters (Fantle and Higgins, 2014), which have undergone only very early diagenesis, are also included. Although there are several additional studies of $\delta^{44/40}$Ca in carbonate rock or core-top sediments, these studies lack data on [Sr] and thus are not useful for this exercise.

The compiled $\delta^{44/40}$Ca data exhibit a correlation with [Sr] similar to the data presented in this study, with a significant inverse correlation (Spearman's $\rho = -0.64$, p-value < 0.001), despite the vast differences in paleogeographic location and time interval. A log-linear SMA regression model (Figure 11B) is statistically better than a linear SMA model (Figure 11A; ΔAIC = -8806; Table A.1). Correlations between $\delta^{44/40}$Ca and Sr/Ca ratios are better modeled using a linear relationship (Figure 11C, D; Table A.1), but the converse is true for correlations with Sr/(Mg+Ca) ratios (Figure 11E, F). However, given the limited number of datasets reporting these ratios, it is unclear what might explain the differences in correlation between [Sr] and normalized [Sr].

The ubiquitous log-linear relationship of $\delta^{44/40}$Ca with [Sr] suggests that the major control on bulk shallow-marine $\delta^{44/40}$Ca composition in carbonates since the Neoproterozoic is a combination of initial carbonate mineralogy and subsequent recrystallization. The individual Ediacaran datasets (Sawaki et al., 2014; Husson et al., 2015), the Triassic/Jurassic carbonates (Jost et al., 2017), and the non-dolomitized Ordovician carbonates (Holmden et al., 2012a) are also better described by a log-linear than a linear regression model (see Table A.1 for statistics). The comparable regression slopes for most of these datasets (that are also similar to the regression for the compilation) may indicate a relatively consistent shallow marine diagenetic regime through time.

There are exceptions to the inverse log-linear correlation that suggest additional local factors played a larger role than early diagenetic recrystallization in determining the $\delta^{44/40}$Ca of carbonate sediments at some sites. First, the positive correlation between Sr/Ca and $\delta^{44/40}$Ca in Middle-Late Ordovician carbonates from Saskatchewan is interpreted as mixing between dolomitized and non-dolomitized end-members (Holmden, 2009). Second, Upper Silurian carbonate $\delta^{44/40}$Ca and [Sr] values fall along a linear mixing line with a slope in agreement with the experimentally determined dependence of the kinetic fractionation factor on the precipitation rate (Farkaš et al., 2016). Finally, there is no significant correlation between $\delta^{44/40}$Ca and [Sr] for the Permian dataset (Jost et al., 2014). Thus, although early diagenetic recrystallization appears to be the dominant control in many published datasets, the influence of many other local factors can become more important and cannot be ignored.

4.5 Implications for interpreting changes in the global Ca cycle

This study highlights the challenges of reconstructing secular variation in seawater $\delta^{44/40}$Ca from bulk carbonate rock samples. In many instances, the expected coupling between C and Ca cycles and their isotopic compositions appears to have been erased or heavily overprinted (Griffith et al., 2015). Our findings demonstrate that the $\delta^{44/40}$Ca of carbonate rocks is controlled by three major processes: the $\delta^{44/40}$Ca of contemporaneous seawater, the proportions of the two major $CaCO_3$ polymorphs, and the degree of resetting during recrystallization. The similarities in the log-linear relationship of $\delta^{44/40}$Ca and [Sr] between our Permian/Triassic records and data spanning selected intervals across the past ~650 million years suggest that the last two factors may have been dominant through the Phanerozoic, and the nearly identical slopes imply that such processes were common from the Late Permian through the Middle Triassic. Because mineralogy and recrystallization greatly influenced bulk carbonate $\delta^{44/40}$Ca, these local effects present a challenge in reconstructing changes in seawater $\delta^{44/40}$Ca using bulk carbonate rock, as these factors may obscure the temporal patterns. For example, the uncorrelated $\delta^{44/40}$Ca data at Dajiang and Taşkent after the Griesbachian substage appear to predominantly reflect local controls.

In samples where mineralogy and recrystallization are the most dominant controls on carbonate $\delta^{44/40}$Ca, it may be possible to account for the effect of variable $CaCO_3$ mineralogy and diagenesis, and broadly estimate secular changes in seawater $\delta^{44/40}$Ca. Seawater [Sr] has undoubtedly changed over the Phanerozoic (Richter et al., 1992; Steuber and Veizer, 2002), and partitioning of Sr into carbonates is a function of organism growth and calcification rate (Stoll and Schrag, 1998) in addition to the $CaCO_3$ polymorph, and thus is variable through time. However, comparing the range of $\delta^{44/40}$Ca values for a given [Sr] should provide a general sense of how seawater $\delta^{44/40}$Ca varied among the studied time intervals. In other words, if partitioning of Sr is assumed to be constant over the Phanerozoic, varying seawater $\delta^{44/40}$Ca would result in vertical shifts in the regression intercept. This intercept does not hold geologic meaning, but can be interpreted as normalized carbonate $\delta^{44/40}$Ca with overprinting of mineralogy and recrystallization removed. Thus, SMA intercepts for each dataset in Figure 11B (assuming a generally similar diagenetic regime such that the data are well-represented by a negative regression) can be compared to each other. Indeed, despite the differences between $\delta^{44/40}$Ca data from Dajiang and Taşkent, their SMA intercepts are similar (Figure 8B), consistent with precipitation from seawater with a shared $\delta^{44/40}$Ca value.

To test this estimation, we used Phanerozoic $\delta^{44/40}$Ca records hypothesized to reflect predominantly aragonite or calcite precipitation, based on Mg/Ca ratios. In the calcitic seas of the early Paleozoic, Mg/Ca ratios and inferred seawater $\delta^{44/40}$Ca values are lower than intervals of aragonitic seas (Blättler et al., 2012; Farkaš et al., 2007; Le Houedec et al., 2017; Stanley, 2006). The regression intercepts of the log-linear models also mirror this trend, suggesting that first-order variations in seawater $\delta^{44/40}$Ca can be preserved in bulk carbonate rocks (Figure 12; Table A.1). For example, the intercept is more negative during the calcitic seas in the Ordovician (Holmden et al., 2009) than for the aragonitic seas in the Triassic to early Jurassic (this study; Jost et al., 2017). The intercepts of Neoproterozoic datasets are more negative than in the Phanerozoic, but it is difficult to test whether this agrees with seawater $\delta^{44/40}$Ca in an inferred calcite seabecause seawater Mg/Ca is less well constrained (Husson et al., 2015; Sawaki et al., 2014). Thus, first-order secular trends in seawater $\delta^{44/40}$Ca may be recovered despite diagenetic overprinting. We caution that at this point, these corrections for mineralogy and recrystallization are only qualitative with large uncertainties (Table A.1), and quantitative estimates are beyond the scope of this paper. Although the assumption made here that partitioning of Sr into carbonates was invariant is simplistic, this assumption and the sensitivity of the result to this assumption are testable in the case that quantitative interpretation is desired.

An important observation of the present study is that the absolute values of $\delta^{44/40}$Ca differ substantially between two coeval stratigraphic sections. Because the 0.3‰ negative shift at the end-Permian extinction boundary is reproduced at geographically disparate areas and between different minerals (Hinojosa et al., 2012), we infer that this excursion reflects a change in seawater chemistry that dominates local and post-depositional factors. However, the absolute values and patterns higher in the section reveal significant heterogeneity in $\delta^{44/40}$Ca and suggest that local factors can make interpretation between stratigraphic sections challenging. The $\delta^{44/40}$Ca record at Dajiang—which is more positive than at Taşkent—is most likely explained by more prevalent aragonite precipitation at Taşkent than at Dajiang, which would result in a larger Δ_{c-s} – reflected by greater [Sr] and more negative $\delta^{44/40}$Ca values. It is probable that the carbonates experienced varying degrees of resetting during recrystallization, as supported by geochemical and petrographic observations. Our findings emphasize the importance of collecting bulk carbonate $\delta^{44/40}$Ca data from multiple stratigraphic sections across geographic areas to evaluate the importance of the many processes that can affect the fidelity of this proxy.

5. CONCLUSIONS

Because fluctuations in seawater $\delta^{44/40}$Ca are primarily influenced by imbalances in the calcium cycle, calcium isotopes hold promise for elucidating patterns in the coupled C and Ca cycles. However, numerous factors can cause the $\delta^{44/40}$Ca value recorded in carbonate sediments and rocks to deviate from the contemporaneous seawater $\delta^{44/40}$Ca composition. In this study, we test the utility of carbonate $\delta^{44/40}$Ca to constrain C and Ca cycling by comparing $\delta^{44/40}$Ca in two stratigraphic sections that span the Upper Permian to Middle Triassic. We do not find covarying shifts in $\delta^{44/40}$Ca in our two sections above the reproducible negative excursion at the Permian/Triassic boundary. Instead, recrystallization and $CaCO_3$ mineralogy both contribute to control the $\delta^{44/40}$Ca value of our bulk carbonates and any signal of changes in seawater $\delta^{44/40}$Ca composition has not been preserved. We suggest that any changes in seawater carbonate chemistry—and the subsequent changes in carbonate $\delta^{44/40}$Ca—were either too small to be preserved, or were overprinted by these other factors. Although other records (*e.g.*, conodonts) may prove useful to providing these constraints in future studies, our results support the hypothesis that δ^{13}C perturbations were not driven by changing carbonate chemistry, but instead changing redox conditions and organic carbon burial (Lau et al., 2016).

Although they appear to show little agreement in absolute $\delta^{44/40}$Ca value as well as temporal trend, they both exhibit the same systematic relationship with [Sr]—specifically, an inverse correlation between log([Sr]) and $\delta^{44/40}$Ca. This log-linear relationship can be explained using a model of water-rock interaction of early diagenetic recrystallization from variable aragonite-to-calcite ratios in the original sediment, precipitated from seawater with the same $\delta^{44/40}$Ca and [Sr]. These factors of original mineralogy and water-rock interaction play a dominant role in the bulk carbonate $\delta^{44/40}$Ca value at these sites. This interpretation is further supported by a comparable relationship between log([Sr]) and $\delta^{44/40}$Ca in compiled core-top shallow-marine carbonate sediments and rocks spanning the past 600 million years. Despite overprinting by local factors, first-order temporal trends in carbonate $\delta^{44/40}$Ca can be informative of seawater chemistry and secular trends in seawater $\delta^{44/40}$Ca may be reconstructed from bulk carbonate records.

Acknowledgements: This research was supported by National Science Foundation Continental Dynamics Grant EAR-0807475, American Chemical Society Petroleum Research Fund Grant 52457-ND2, and National Aeronautics and Space Administration Grant NNX09AN67G to J.L.P., and an ARCS Fellowship, the GSA Gretchen L. Blechschmidt Award, and the AAPG David Worthington Named Grant to K.V.L. The isotopic spike used in this research was supplied by the United States Department of Energy Office of Science by the Isotope Program in the Office of Nuclear Physics. We thank Guangchao Li, Tom Owens, and Hailun (Cindy) Ni for assistance in the laboratory, and three anonymous reviewers for helpful suggestions that improved this manuscript.

References

Algeo, T.J., Hinnov, L., Moser, J., Maynard, J.B., Elswick, E., Kuwahara, K., Sano, H., 2010. Changes in productivity and redox conditions in the Panthalassic Ocean during the latest Permian. Geology 38, 187-190.

Algeo, T.J., Henderson, C.M., Tong, J., Feng, Q., Yin, H., Tyson, R.V., 2013. Plankton and productivity during the Permian–Triassic boundary crisis: An analysis of organic carbon fluxes. Global and Planetary Change 105, 52-67.

Algeo, T.J., Kuwahara, K., Sano, H., Bates, S., Lyons, T., Elwsick, E., Hinnov, L., Ellwood, B., Moser, J., Maynard, J.B., 2011. Spatial variation in sediment fluxes, redox conditions, and productivity in the Permian-Triassic Panthalassic Ocean. Palaeogeography, Palaeoclimatology, Palaeoecology 308, 65-83.

AlKhatib, M., Eisenhauer, A., 2017. Calcium and strontium isotope fractionation in aqueous solutions as a function of temperature and reaction rate; I. Calcite. Geochimica et Cosmochimica Acta 209, 296-319.

AlKhatib, M., Eisenhauer, A., 2017. Calcium and strontium isotope fractionation during precipitation from aqueous solutions as a function of temperature and reaction rate; II. Aragonite. Geochimica et Cosmochimica Acta 209, 320-342.

Altiner, D., Özgül, N., 2001. Carboniferous and Permian of the allochthonous terranes of the CentralTauride Belt, southern Turkey, PaleoForams 2001, International Conference on Paleozoic Benthic Foraminifera, 20-24 August 2001, Guidebook., Ankara, p. 35.

Amini, M., Eisenhauer, A., Böhm, F., Fietzke, J., Bach, W., Garbeschonberg, D., Rosner, M., Bock, B., Lackschewitz, K., Hauff, F., 2008. Calcium isotope ($\delta^{44/40}$Ca) fractionation along hydrothermal pathways, Logatchev field (Mid-Atlantic Ridge, 14°45′ N). Geochimica et Cosmochimica Acta 72, 4107-4122.

Atudorei, V., 1999. Constraints on the Upper Permian to Upper Triassic marine carbon isotope curve, Case studies from the Tethys. University of Lausanne, p. 160.

Banner, J.L., Hanson, G.N., 1990. Calculation of simultaneous isotopic and trace element variations during water-rock interaction with applications to carbonate diagenesis. Geochimica et Cosmochimica Acta 54, 3123-3137.

Baud, A., Richoz, S., Pruss, S., 2007. The lower Triassic anachronistic carbonate facies in space and time. Global and Planetary Change 55, 81-89.

Bergmann, K.D., Grotzinger, J.P., Fischer, W.W., 2013. Biological Influences on Seafloor Carbonate Precipitation. Palaios 28, 99-115.

Berner, 1980. Early Diagenesis: A Theoretical Approach. Princeton University Press.

Blättler, C.L., Henderson, G.M., Jenkyns, H.C., 2012. Explaining the Phanerozoic Ca isotope history of seawater. Geology 40, 843-846.

Blättler, C.L., Jenkyns, H.C., Reynard, L.M., Henderson, G.M., 2011. Significant increases in global weathering during Oceanic Anoxic Events 1a and 2 indicated by calcium isotopes. Earth and Planetary Science Letters 309, 77-88.

Böhm, F., Gussone, N., Eisenhauer, A., Dullo, W.-C., Reynaud, S., Paytan, A., 2006. Calcium isotope fractionation in modern scleractinian corals. Geochimica et Cosmochimica Acta 70, 4452-4462.

Brand, U., Veizer, J., 1980. Chemical Diagenesis of a Multicomponent Carbonate System--1: Trace Elements. Journal of Sedimentary Petrology 50, 1219-1236.

Brayard, A., Bucher, H., Escarguel, G., Flueau, F., Bourquin, S., Galfetti, T., 2006. The Early Triassic ammonoid recovery: Paleoclimatic significance of diversity gradients. Palaeogeogrpahy, Palaeoclimatology, Palaeoecology 239, 374-395.

Brayard, A., Escarguel, G., Bucher, H., Monnet, C., Brühwiler, T., Goudemand, N., Galfetti, T., Guex, J., 2009. Good Genes and Good Luck: Ammonoid Diversity and the End-Permian Mass Extinction. Science 325, 1118-1121.

Brazier, J.-M., Suan, G., Tacail, T., Simon, L., Martin, J.E., Mattioli, E., Balter, V., 2015. Calcium isotope evidence for dramatic increase of continental weathering during the Toarcian oceanic anoxic event (Early Jurassic). Earth and Planetary Science Letters 411, 164-176.

Brennecka, G.A., Herrmann, A.D., Algeo, T.J., Anbar, A.D., 2011. Rapid expansion of oceanic anoxia immediately before the end-Permian mass extinction. Proceedings of the National Academy of Sciences 108, 17631-17634.

Brown, S.T., Kennedy, B.M., DePaolo, D.J., Hurwitz, S., Evans, W.C., 2013. Ca, Sr, O and D isotope approach to defining the chemical evolution of hydrothermal fluids: Example from Long Valley, CA, USA. Geochimica et Cosmochimica Acta 122, 209-225.

Burgess, S.D., Bowring, S.A., 2015. High-precision geochronology confirms voluminous magmatism before, during, and after Earth's most severe extinction. Science Advances 1, 1-14.

Chen, Y., Twitchett, R.J., Jiang, H., Richoz, S., Lai, X., Yan, C., Sun, Y., Liu, X., Wang, L., 2013. Size variation of conodonts during the Smithian-Spathian (Early Triassic) global warming event. Geology 41, 823-826.

Chen, Z.-Q., Benton, M.J., 2012. The timing and pattern of biotic recovery following the end-Permian mass extinction. Nature Geoscience 5, 375-383.

Clapham, M.E., Payne, J.L., 2011. Acidification, anoxia, and extinction: A multiple logistic regression analysis of extinction selectivity during the Middle and Late Permian. Geology 39, 1059-1062.

Clarkson, M.O., Kasemann, S.A., Wood, R.A., Lenton, T.M., Daines, S.J., Richoz, S., Ohnemueller, F., Meixner, A., Poulton, S.W., Tipper, E.T., 2015. Ocean acidification and the Permo-Triassic mass extinction. Science 348, 229-232.

Cui, Y., Kump, L.R., Ridgwell, A., 2013. Initial assessment of the carbon emission rate and climatic consequences during the end-Permian mass extinction. Palaeogeography, Palaeoclimatology, Palaeoecology 389, 128-136.

DePaolo, D.J., 2004. Calcium Isotopic Variations Produced by Biological, Kinetic, Radiogenic and Nucleosynthetic Processes. Reviews in Mineralogy 55, 255-288.

DePaolo, D.J., 2011. Surface kinetic model for isotopic and trace element fractionation during precipitation of calcite from aqueous solutions. Geochimica et Cosmochimica Acta 75, 1039-1056.

De La Rocha, C.L., DePaolo, D.J., 2000. Isotopic Evidence for Variations in the Marine Calcium Cycle Over the Cenozoic. Science 289, 1176-1178.

Du Vivier, A.D.C., Jacobson, A.D., Lehn, G.O., Selby, D., Hurtgen, M.T., Sageman, B.B., 2015. Ca isotope stratigraphy across the Cenomanian–Turonian OAE 2: Links between volcanism, seawater geochemistry, and the carbonate fractionation factor. Earth and Planetary Science Letters 416, 121-131.

Enos, P., Sawatsky, LH., 1981. Pore networks in Holocene carbonate sediments. Journal of Sedimentary Petrology 51, 961-985.

Fantle, M.S., 2010. Evaluating the Ca isotope proxy. American Journal of Science 310, 194-230.

Fantle, M.S., 2015. Calcium isotopic evidence for rapid recrystallization of bulk marine carbonates and implications for geochemical proxies. Geochimica et Cosmochimica Acta 148, 378-401.

Fantle, M.S., DePaolo, D.J., 2005. Variations in the marine Ca cycle over the past 20 million years. Earth and Planetary Science Letters 237, 102-117.

Fantle, M.S., DePaolo, D.J., 2007. Ca isotopes in carbonate sediment and pore fluid from ODP Site 807A: The Ca^{2+}(aq)–calcite equilibrium fractionation factor and calcite recrystallization rates in Pleistocene sediments. Geochimica et Cosmochimica Acta 71, 2524-2546.

Fantle, M.S., Higgins, J., 2014. The effects of diagenesis and dolomitization on Ca and Mg isotopes in marine platform carbonates: Implications for the geochemical cycles of Ca and Mg. Geochimica et Cosmochimica Acta 142, 458-481.

Fantle, M.S., Maher, K.M., DePaolo, D.J., 2010. Isotopic approaches for quantifying the rates of marine burial diagenesis. Reviews of Geophysics 48.

Fantle, M.S., Tipper, E.T., 2014. Calcium isotopes in the global biogeochemical Ca cycle: Implications for development of a Ca isotope proxy. Earth-Science Reviews 129, 148-177.

Farkaš, J., Böhm, F., Wallmann, K., Blenkinsop, J., Eisenhauer, A., Vangeldern, R., Munnecke, A., Voigt, S., Veizer, J., 2007. Calcium isotope record of Phanerozoic oceans: Implications for chemical evolution of seawater and its causative mechanisms. Geochimica et Cosmochimica Acta 71, 5117-5134.

Farkaš, J., Frýda, J., Holmden, C., 2016. Calcium isotope constraints on the marine carbon cycle and $CaCO_3$ deposition during the late Silurian (Ludfordian) positive $\delta^{13}C$ excursion. Earth and Planetary Science Letters 451, 31-40.

Farkaš, J., Frýda, J., Holmden, C., 2017. Corrigendum to "Calcium isotope constraints on the marine carbon cycle and $CaCO_3$ deposition during the late Silurian (Ludforidan) positive $\delta^{13}C$ excursion". Earth and Planetary Science Letters, in press.

Foster, W.J., Twitchett, R.J., 2014. Functional diversity of marine ecosystems after the Late Permian mass extinction event. Nature Geoscience 7, 233-238.

Georgiev, S., Stein, H.J., Hannah, J.L., Bingen, B., Weiss, H.M., Piasecki, S., 2011. Hot acidic Late Permian seas stifle life in record time. Earth and Planetary Science Letters 310, 389-400.

Goddéris, Y., François, L.M., 1995. The Cenozoic evolution of the strontium and carbon cycles: relative importance of continental erosion and mantle exchange. Chemical Geology 126, 169-190.

Gothmann, A.M., Bender, M.L., Blättler, C.L., Swart, P.K., Giri, S.J., Adkins, J.F., Stolarski, J., Higgins, J.A., 2016. Calcium isootpes in scleractinian fossil corals since the Mesozoic: Implications for vital effects and biomineralization through time. Earth and Planetary Science Letters 444, 205-214.

Griffith, E.M., Fantle, M.S., Eisenhauer, A., Paytan, A., Bullen, T.D., 2015. Effects of ocean acidification on the marine calcium isotope record at the Paleocene–Eocene Thermal Maximum. Earth and Planetary Science Letters 419, 81-92.

Griffith, E.M., Paytan, A., Caldeira, K., Bullen, T., Thomas, E., 2008. A Dynamic Marine Calcium Cycle During the Past 28 Million Years. Science 322, 1671-1674.

Griffith, E.M., Paytan, A., Eisenhauer, A., Bullen, T.D., Thomas, E., 2011. Seawater calcium isotope ratios across the Eocene-Oligocene transition. Geology 39, 683-686.

Groves, J.R., Altiner, D., Rettori, R., 2005. Extinction, survival, and recovery of Langenide foraminifers in the Permian-Triassic boundary interval, Central Taurides, Turkey. Journal of Paleontology 79, 1-38.

Gussone, N., Böhm, F., Eisenhauer, A., Dietzel, M., Heuser, A., Teichert, B., Reitner, J., Worheide, G., Dullo, W.,

2005. Calcium isotope fractionation in calcite and aragonite. Geochimica et Cosmochimica Acta 69, 4485-4494.

Hallam, A., 1991. Why was there a delayed radiation after the end-Paleozoic extinctions? Historical Biology 5, 257-262.

Heuser. A., Eisenhauer, A., Böhm, F., Wallmann, K., Gussone, N., Pearson, P.N., Nägler, T.F., Dullo, W.-C., 2005. Calcium isotope (δ^{44}Ca) variations of Neogene plantkonic foraminifera. Paleoceanography 20, 1-13.

Heuser, A., Eisenhauer, A., Gussone, N., Bock, B., Hansen, B.T., Nagler, T.F., 2002. Measurement of calcium isotopes (δ^{44}Ca) using a multicollector TIMS technique. International Journal of Mass Spectrometry 230, 385-397.

Higgins, J.A., Fischer, W.W., Schrag, D.P., 2009. Oxygenation of the ocean and sediments: Consequences for the seafloor carbonate factory. Earth and Planetary Science Letters 284, 25-33.

Hinojosa, J.L., Brown, S.T., Chen, J., DePaolo, D.J., Paytan, A., Shen, S.z., Payne, J.L., 2012. Evidence for end-Permian ocean acidification from calcium isotopes in biogenic apatite. Geology 40, 743-746.

Hippler, D., Kozdon, R., Darling, K.F., Eisenhauer, A., Nägler, T.F., 2009. Calcium isotopic composition of high-latitude proxy carrier *Neogloboquadrina pachyderma* (sin.). Biogeosciences 6, 1-14.

Holmden, C., 2009. Ca isotope study of Ordovician dolomite, limestone, and anhydrite in the Williston Basin: Implications for subsurface dolomitization and local Ca cycling. Chemical Geology 268, 180-188.

Holmden, C., Panchuk, K., Finney, S.C., 2012a. Tightly coupled records of Ca and C isotope changes during the Hirnantian glaciation event in an epeiric sea setting. Geochimica et Cosmochimica Acta 98, 94-106.

Holmden, C., Papanastassiou, D.A., Blanchon, P., Evans, S., 2012b. $\delta^{44/40}$Ca variability in shallow water carbonates and the impact of submarine groundwater discharge on Ca-cycling in marine environments. Geochimica et Cosmochimica Acta 83, 179-194.

Horacek, M., Brandner, R., Abart, R., 2007a. Carbon isotope record of the P/T boundary and the Lower Triassic in the Southern Alps: Evidence for rapid changes in storage of organic carbon. Palaeogeography, Palaeoclimatology, Palaeoecology 252, 347-354.

Horacek, M., Richoz, S., Brandner, R., Krystyn, L., Spötl, C., 2007b. Evidence for recurrent changes in Lower Triassic oceanic circulation of the Tethys: The δ^{13}C record from marine sections in Iran. Palaeogeography, Palaeoclimatology, Palaeoecology 252, 355-369.

Husson, J.M., Higgins, J.A., Maloof, A.C., Schoene, B., 2015. Ca and Mg isotope constraints on the origin of Earth's deepest δ^{13}C excursion. Geochimica et Cosmochimica Acta 160, 243-266.

Jacobson, A.D. and Holmden, C., 2008. δ^{44}Ca evolution in a carbonate aquifer and its bearing on the equilibrium isotope fractionation factor for calcite. Earth and Planetary Science Letters 270, 349-353.

Jones, G.D., Whitaker, F.F., Smart, P.L., Sanford, W.E., 2006. Fate of reflux brines in carbonate platforms. Geology 2002 30, 371-374.

Jones, G.D., Xiao, Y., 2015. Dolomitization, anhydrite cementation, and porosity evolution in a reflux system: Insights from reactive transport models. AAPG Bulletic 89, 577-601.

Jost, A.B., Bachan, A., van de Schootbrugge, B., Brown, S.T., DePaolo, D.J., Payne, J.L., 2017. Additive effects of acidification and mineralogy on calcium isotopes in Triassic/Jurassic boundary limestones. Geochemistry, Geophyscis, Geosystems 18, 113-124.

Jost, A.B., Mundil, R., He, B., Brown, S.T., Altiner, D., Sun, Y., DePaolo, D.J., Payne, J.L., 2014. Constraining the cause of the end-Guadalupian extinction with coupled records of carbon and calcium isotopes. Earth and Planetary Science Letters 396, 201-212.

Kasemann, S.A., Pogge von Strandmann, P.A.E., Prave, A.R., Fallick, A.E., Elliott, T., Hoffmann, K.-H., 2014. Continental weathering following a Cryogenian glaciation: Evidence from calcium and magnesium isotopes. Earth and Planetary Science Letters 396, 66-77.

Kaufman, A.J., Jacobsen, S.B., Knoll, A.H., 1993. The Vendian record of Sr and C isotopic variations in seawater: Implications for tectonics and paleoclimate. Earth and Planetary Science Letters 120, 409-430.

Kaufman, J., 1994. Numerical models of fluid flow in carbonate platforms: Implications for dolomitization. Journal of Sedimentary Research A64, 128-139.

Kiessling, W., Simpson, C., 2011. On the potential for ocean acidification to be a general cause of ancient reef crises. Global Change Biology 17, 56-67.

Kimmig, S.R., Holmden, C., 2017. Multi-proxy geochemical evidence for primary aragonite precipitation in a tropical-shelf 'calcite sea' during the Hirnantian glaciation. Geochimica et Cosmochimica Acta 206, 254-272.

Kinsman, D.J., 1969. Interpretation of Sr+2 Concentrations in Carbonate Minerals and Rocks. Journal of Sedimentary Petrology 39, 486-508.

Knoll, A.H., Bambach, R.K., Payne, J.L., Pruss, S., Fischer, W.W., 2007. Paleophysiology and end-Permian mass extinction. Earth and Planetary Science Letters 256, 295-313.

Komar, N., Zeebe, R.E., 2016. Calcium and calcium isotope changes during carbon cycle perturbations at the end-Permian. Paleoceanography 31, 115-130.

Krull, E.S., Lehrmann, D.J., Druke, D., Kessel, B., Yu, Y., Li, R., 2004. Stable carbon isotope stratigraphy across the Permian–Triassic boundary in shallow marine carbonate platforms, Nanpanjiang Basin, south China. Palaeogeography, Palaeoclimatology, Palaeoecology 204, 297-315.

Kump, L.R., 1989. Alternative Modeling Approaches to the Geochemical Cycles of Carbon, Sulfur, and Strontium Isotopes. American Journal of Science 289, 390-410.

Land, L.S., 1985. The Origin of Massive Dolomite. Journal of Geological Education 33, 112-125.

Lau, K.V., Maher, K., Altiner, D., Kelley, B.M., Kump, L.R., Lehrmann, D.J., Silva-Tamayo, J.C., Weaver, K.L., Yu, M., Payne, J.L., 2016. Marine anoxia and delayed Earth system recovery after the end-Permian extinction. Proceedings of the National Academy of Sciences 113, 2360-2365.

Lau, K.V., Macdonald, F.A., Maher, K., Payne, J.L., 2017. Uranium isotope evidence for temporary ocean oxygenation in the aftermath of the Sturtian Snowball Earth. Earth and Planetary Science Letters 458, 282-292.

Le Houedec, S., McCulloch, M., Trotter, J., Rankenburg, K. Conodont apatite $\delta^{88/86}$Sr and $\delta^{44/40}$Ca compositions and implications for the evolution of Palaeozoic to early Mesozoic seawater. Chemical Geology 453, 55-65.

Lehrmann, D.J., Donghong, P., Enos, P., Minzoni, M., Ellwood, B.B., Orchard, M.J., Jiyan, Z., Jiayong, W., Dillett, P., Koenig, J., Steffen, K., Druke, D., Druke, J., Kessel, B., Newkirk, T., 2007. Impact of differential tectonic subsidence on isolated carbonate-platform evolution: Triassic of the Nanpanjiang Basin, south China. AAPG Bulletin 91, 287-320.

Lehrmann, D.J., Enos, P., Payne, J.L., Montgomery, P., Wei, J., Yu, Y., Xiao, J., Orchard, M.J., 2005. Permian and Triassic depositional history of the Yangtze platform and Great Bank of Guizhou in the Nanpanjiang basin of Guizhou and Guangxi, south China. Albertiana 33, 167-184.

Lehrmann, D.J., Minzoni, M., Li, X., Yu, M., Payne, J.L., Kelley, B.M., Schaal, E.K., Enos, P., 2012. Lower Triassic oolites of the Nanpanjiang Basin, south China: Facies architecture, giant ooids, and diagenesis—Implications for hydrocarbon reservoirs. AAPG Bulletin 96, 1389-1414.

Lehrmann, D.J., Payne, J.L., Felix, S.V., Dillett, P.M., Wang, H., Yu, Y.Y., and Wei, J.Y., 2003. Permian-Triassic boundary setions from shallow-marine carbonate platforms of the Nanpanjiang basin, south China: Implications for ocenaic conditions associated with the end-Permian extinction and its aftermath. Palaios 18, 138-152.

Lehrmann, D.J., Ramezani, J., Bowring, S.A., Martin, M.W., Montgomery, P., Enos, P., Payne, J.L., Orchard, M.J., Hongmei, W., Jiayong, W., 2006. Timing of recovery from the end-Permian extinction: Geochronologic and biostratigraphic constraints from south China. Geology 34, 1053.

Lehrmann, D.J., Stepchinski, L., Altiner, D., Orchard, M.J., Montgomery, P., Enos, P., Ellwood, B.B., Bowring, S.A., Ramezani, J., Wang, H., 2015. An integrated biostratigraphy (conodonts and foraminifers) and chronostratigraphy (paleomagnetic reversals, magnetic susceptibility, elemental chemistry, carbon isotopes and geochronology) for the Permian–Upper Triassic strata of Guandao section, Nanpanjiang Basin, south China. Journal of Asian Earth Sciences 108, 117-135.

Lehrmann, D.J., Wan, Y., Wei, J., Yu, Y., Xiao, J., 2001. Lower Triassic peritidal cyclic limestone: an example of anachronistic carbonate facies from the Great Bank of Guizhou, Nanpanjiang Basin, Guizhou province, South China. Palaeogeography, Palaeoclimatology, Palaeoecology 173, 103-123.

Lehrmann, D.J., Wei, J., Enos, P., 1998. Controls on Facies Architecture of a Large Triassic Carbonate Platform: The Great Bank of Guizhou, Nanpanjiang Basin, South China. Journal of Sedimentary Research 68, 311-326.

Lemarchand, D., Wasserbug, G.J., Papanastassiou, D.A., 2004. Rate-controlled calcium isotope fractionation in synthetic calcite. Geochimica et Cosmochimica Acta 68, 4665-4678.

Li, X., Yu, M., Lehrmann, D.J., Payne, J.L., Kelley, B.M., Minzoni, M., 2012. Factors controlling carbonate platform asymmetry: Preliminary results from the Great Bank of Guizhou, an isolated Permian–Triassic Platform in the Nanpanjiang Basin, south China. Palaeogeography, Palaeoclimatology, Palaeoecology 315-316, 158-171.

Loyd, S.J., Berelson, W.M., Lyons, T.W., Hammond, D.E., Corsetti, F.A., 2012. Constraining pathways of microbial mediation for carbonate concretions of the Miocene Monterey Formation using carbonate-associated sulfate. Geochimica et Cosmochimica Acta 78, 77-98.

Machel, H.G., 1997. Recrystallization versus neomorphism, and the concept of 'significant recrystallization' in dolomite research. Sedimentary Geology 113, 161-168.

Maher, K., Steefel, C.I., DePaolo, D.J., Viani, B.E., 2006. The mineral dissolution rate conundrum: Insights from reactive transport modeling of U isotopes and pore fluid chemistry in marine sediments. Geochimica et Cosmochimica Acta 70, 337-363.

Marriott, C.S., Henderson, G.M., Belshaw, N.S., Tudhope, A.W., 2004. Temperature dependence of δ^{7}Li, δ^{44}Ca and Li/Ca during growth of calcium carbonate. Earth and Planetary Science Letters 222, 615-624.

Meyer, K.M., Yu, M., Jost, A.B., Kelley, B.M., Payne, J.L., 2011. δ^{13}C evidence that high primary productivity delayed recovery from end-Permian mass extinction. Earth and Planetary Science Letters 302, 378-384.

Minzoni, M., Lehrmann, D.J., Payne, J.L., Enos, P., Yu, M., Wei, J., Kelley, B.M., Li, X., Schaal, E., Meyer, K.M., Montgomery, P., Goers, A., Wood, T., 2013. Triassic Tank: Platform Margin and Slope Architecture in Space and Time, Nanpanjiang Basin, South China. SEPM Special Publication 105, 84-113.

Monod, O., 1977. Recherches géologiques dans le Taurus occidental au Sud de Beysehir (Turquie) [Ph.D. thesis]. Université de Paris-Sud, Centre d'Orsay, p. 442.

Moore, C.H., 1989. Carbonate Diagenesis and Porosity. Developments in Sedimentology Vol. 46. Elsevier Science Publishing B.V.

Nielsen, L.C., De Yoreo, J.J., DePaolo, D.J., 2013. General model for calcite growth kinetics in the presence of impurity ions. Geochimica et Cosmochimica Acta 115, 100-114.

Nielsen, L.C., DePaolo, D.J., De Yoreo, J.J., 2012. Self-consistent ion-by-ion growth model for kinetic isotopic fractionation during calcite precipitation. Geochimica et Cosmochimica Acta 86, 166-181.

Orchard, M.J., 2007. Conodont diversity and evolution through the latest Permian and Early Triassic upheavals. Palaeogeography, Palaeoclimatology, Palaeoecology 252, 93-117.

Özgül, N., 1997. Stratigraphy of the tectono-stratigraphic units in the region Bozkir-Hadim-Taşkent (northern central Taurides) [in Turkish with English abstract]. Mineral Research and Exploration Institute of Turkey (MTA) Bulletin 119, 113-174.

Payne, J.L., Kump, L., 2007. Evidence for recurrent Early Triassic massive volcanism from quantitative interpretation of carbon isotope fluctuations. Earth and Planetary Science Letters 256, 264-277.

Payne, J.L., Lehrmann, D.J., Christensen, S., Wei, J., Knoll, A.H., 2006a. Environmental and Biological Controls on the Initiation and Growth of a Middle Triassic (Anisian) Reef on the Great Bank of Guizhou, Guizhou Province, China. Palaios 21, 325-343.

Payne, J.L., Lehrmann, D.J., Follett, D., Seibel, M., Kump, L.R., Riccardi, A., Altiner, D., Sano, H., Wei, J., 2007. Erosional truncation of uppermost Permian shallow-marine carbonates and implications for Permian-Triassic boundary events. Geological Society of America Bulletin 119, 771-784.

Payne, J.L., Lehrmann, D.J., Wei, J., Knoll, A.H., 2006b. The Pattern and Timing of Biotic Recovery from the End-Permian Extinction on the Great Bank of Guizhou, Guizhou Province, China. Palaios 21, 63-85.

Payne, J.L., Lehrmann, D.J., Wei, J., Orchard, M.J., Schrag, D.P., Knoll, A.H., 2004. Large perturbations of the carbon cycle during recovery from the end-Permian extinction. Science 305, 506-509.

Payne, J.L., Summers, M., Rego, B.L., Altiner, D., Wei, J., Yu, M., Lehrmann, D.J., 2011. Early and Middle Triassic trends in diversity, evenness, and size of foraminifers on a carbonate platform in south China: implications for tempo and mode of biotic recovery from the end-Permian mass extinction. Paleobiology 37, 409-425.

Payne, J.L., Turchyn, A.V., Paytan, A., DePaolo, D.J., Lehrmann, D.J., Yu, M., Wei, J., 2010. Calcium isotope constraints on the end-Permian mass extinction. Proceedings of the National Academy of Sciences 107, 8543.

Pruss, S.B., Bottjer, D.J., Corsetti, F.A., Baud, A., 2006. A global marine sedimentary response to the end-Permian mass extinction: Examples from southern Turkey and the western United States. Earth-Science Reviews 78, 193-206.

Richoz, S., 2006. Stratigraphie et variations isotopiques du carbone dans le Permien supérieur et le Trias inférieur de quelques localités de la Néotéthys (Turquie, Oman et Iran), Institut de Géologie et Paléontologie. Univeristé de Lausanne, Lausanne, Suitzerland, p. 284.

Richter, F.M., Rowley, D.B., DePaolo, D., 1992. Sr isotope evolution of seawater: the role of tectonics. Earth and Planetary Science Letters 109, 11-23.

Romano, C., Goudemand, N., Vennemann, T.W., Ware, D., Schneebeli-Hermann, E., Hochuli, P.A., Bruhwiler, T., Brinkmann, W., Bucher, H., 2013. Climatic and biotic upheavals following the end-Permian mass extinction. Nature Geoscience 6, 57-60.

Sawaki, Y., Tahata, M., Ohno, T., Komiya, T., Hirata, T., Maruyama, S., Han, J., Shu, D., 2014. The anomalous Ca cycle in the Ediacaran ocean: Evidence from Ca isotopes preserved in carbonates in the Three Gorges area, South China. Gondwana Research 25, 1070-1089.

Schaal, E.K., 2014. Permian-Triassic Global Change: The Strontium Cycle and Body Size Evolution in Marine Clades. Ph.D. dissertation, Stanford University.

Schaal, E.K., Clapham, M.E., Rego, B.L., Wang, S.C., Payne, J.L., 2016. Comparative size evolution of marine clades from the Late Permian through Middle Triassic. Paleobiology 42, 127-142.

Schmitt, A.-D., Chabaux, F., Stille, P., 2003. The calcium riverine and hydrothermal isotopic fluxes and the oceanic calcium mass balance. Earth and Planetary Science 213, 503-518.

Silva-Tamayo, J.C., Nägler, T.F., Sial, A.N., Nogueira, A., Kyser, K., Riccomini, C., James, N.P., Narbonne, G.M., Villa, I.M., 2010a. Global perturbation of the marine Ca isotopic composition in the aftermath of the Marinoan global glaciation. Precambrian Research 182, 373-381.

Silva-Tamayo, J.C., Nägler, T.F., Villa, I.M., Kyser, K., Vieira, L.C., Sial, A.N., Narbonne, G.M., James, N.P., 2010b. Global Ca isotope variations in c. 0.7 Ga old post-glacial carbonate successions. Terra Nova 22, 188-194.

Silva-Tamayo, J.C., Lau, K.V., Jost, A.B., Payne, J.L., Wignall, P.B., Newton, R.J., Eisenhauer, A., DePaolo, D.J., Brown, S.T., Maher, K., Lehrmann, D.J., Altiner, D., Yu, M., Richoz, S., Paytan, A., accepted. Global Perturbation of the Marine Calcium Cycle During the Permian-Triassic Transition. GSA Bulletin.

Sime, N.G., De La Rocha, C.L., Galy, A., 2005. Negligible temperature dependence of calcium isotope fractionation in 12 species of planktonic formainifera. Earth and Planetary Science Letters 232, 51-66.

Sime, N.G., De La Rocha, C.L., Tipper, E.T., Tripati, A., Galy, A., Bickle, M., 2007. Interpreting the Ca isotope record of marine biogenic carbonates. Geochimica et Cosmochimica Acta 71, 3979-3989.

Simms, M., 1984. Dolomitization by groundwater-flow systems in carbonate platforms. AAPG Bulletin 34, 411-420.

Skulan, J., DePaolo, D., Owens, T.L., 1997. Biological control of calcium isotopic abundances in the global calcium cycle. Geochimica et Cosmochimica Acta 61, 2505-2510.

Song, H.-J., Tong, J., Xiong, Y., Sun, D., Tian, L., Song, H.-Y., 2012a. The large increase of δ^{13}C carb-depth gradient and the end-Permian mass extinction. Science China Earth Sciences 55, 1101-1109.

Song, H.-J., Wignall, P.B., Chen, Z.-Q., Tong, J., Bond, D.P.G., Lai, X., Zhao, X., Jiang, H., Yan, C., Niu, Z., Chen, J., Yang, H., Wang, Y., 2011. Recovery tempo and pattern of marine ecosystems after the end-Permian mass extinction. Geology 39, 739-742.

Song, H.-J., Wignall, P.B., Tong, J., Yin, H., 2012b. Two pulses of extinction during the Permian-Triassic crisis. Nature Geoscience 6, 52-56.

Song, H.-Y., Tong, J., Algeo, T.J., Horacek, M., Qiu, H., Song, H.-J., Tian, L., Chen, Z.-Q., 2013. Large vertical $\delta^{13}C_{DIC}$ gradients in Early Triassic seas of the South China craton: Implications for oceanographic changes related to Siberian Traps volcanism. Global and Planetary Change 105, 7-20.

Song, H.-Y., Tong, J., Algeo, T.J., Song, H.-J., Qiu, H., Zhu, Y., Tian, L., Bates, S., Lyons, T.W., Luo, G., Kump, L.R., 2014. Early Triassic seawater sulfate drawdown. Geochimica et Cosmochimica Acta 128, 95-113.

Stanley, S.M., 2006. Influence of seawater chemistry on biomineralization throughout Phanerozoic time: Paleontological and experimental evidence. Palaeogeography, Palaeoclimatology, Palaeoecology 232, 214-236.

Stanley, S.M., 2009. Evidence from ammonoids and conodonts for multiple Early Triassic mass extinctions. Proceedings of the National Academy of Sciences 106, 15264-15267.

Steuber, T., Buhl, D., 2006. Calcium-isotope fractionation in selected modern and ancient marine carbonates. Geochimica et Cosmochimica Acta 70, 5507-5521.

Steuber, T., Veizer, J., 2002. Phanerozoic record of plate tectonic control of seawater chemistry and carbonate sedimentation. Geology 30, 1123-1126.

Stoll, H.M., Schrag, D.P., 1998. Effects of Quaternary sea level cycles on strontium in seawater. Geochimica et Cosmochimica Acta 62, 1107-1118.

Sun, Y., Joachimski, M.M., Wignall, P.B., Yan, C., Chen, Y., Jiang, H., Wang, L., Lai, X., 2012. Lethally hot temperatures during the Early Triassic greenhouse. Science 338, 366-370.

Svensen, H., Planke, S., Polozov, A.G., Schmidbauer, N., Corfu, F., Podladchikov, Y.Y., Jamtveit, B., 2009. Siberian gas venting and the end-Permian environmental crisis. Earth and Planetary Science Letters 277, 490-500.

Tang, J., Dietzel, M., Böhm, F., Köhler, S.J., Eisenhauer, A., 2008a. Sr^{2+}/Ca^{2+} and $^{44}Ca/^{40}Ca$ fractionation during inorganic calcite formation: II. Ca isotopes. Geochimica et Cosmochimica Acta 72, 3733-3745.

Tang, J., Köhler, S.J., Dietzel, M., 2008b. Sr^{2+}/Ca^{2+} and $^{44}Ca/^{40}Ca$ fractionation during inorganic calcite formation: I. Sr incorporation. Geochimica et Cosmochimica Acta 72, 3718-3732.

Teichert, B.M.A., Gussone, N., Torres, M.E., 2009. Controls on calcium isotope fractionation in sedimentary porewaters. Earth and Planetary Science Letters 279, 373-382.

Tipper, E.T., Galy, A., Bickle, M.J., 2008. Calcium and magnesium isotope systematics in rivers draining the Himalaya-Tibetan-Plateau region: Lithological or fractionation control? Geochimica et Cosmochimica Acta 72, 1057-1075.

Tucker, M.E., Wright, V.P., 1990. Carbonate Sedimentology. Blackwell Scientific Publications, Oxford.

Walter, L.M., Morse, J.W., 1984. Reactive surface area of skeletal carbonates during dissolution: Effect of grain size. Journal of Sedimentary Petrology 54, 1081-1090.

Watkins, J.M., DePaolo, D.J., Watson, E.B., 2017. Kinetic fractionation of non-traditional stable isotopes by diffusion and crystal growth reactions. Reviews in Mineralogy and Geochemistry, 82.

Weidlich, O., Bernecker, M., 2011. Biotic carbonate precipitation inhibited during the Early Triassic at the rim of the Arabian Platform (Oman). Palaeogeography, Palaeoclimatology, Palaeoecology 308, 129-150.

Whitaker, F.F., Smart, P.L., 1990. Active circulation of saline ground waters in carbonate platforms: Evidence from the Great Bahama Bank. Geology 18, 200-203.

Woods, A.D., Bottjer, D.J., Mutti, M., Morrison, J., 1999. Lower Triassic large sea-floor carbonate cements: Their origin and a mechanism for the prolonged biotic recovery from the end-Permian mass extinction. Geology 27, 645-648.

Woods, A.D., 2014. Assessing Early Triassic paleoceeanographic conditions via unusual sedimentary fabrics and features. Earth-Science Reviews 137, 6-18.

Figure captions

Figure 1: Geologic setting. (A) Latest Permian-earliest Triassic paleogeographic locations for Dajiang (south China) and Taşkent (Turkey). (B) Cross section of the Great Bank of Guizhou, south China, showing simplified lithology and location of the Dajiang stratigraphic section in the platform interior. Modified from Lehrmann et al. (1998).

Figure 2: Dajiang stratigraphic section showing δ^{13}C data relative to Vienna Pee Dee Belemnite (VPDB) and $\delta^{44/40}$Ca data relative to bulk silicate earth (BSE) and SRM-915a. Smoothing curve and confidence interval are produced using a spline smoothing fit and a Monte Carlo procedure. $\delta^{44/40}$Ca error bars are 2σ from multiple analyses of the same sample. δ^{13}C data were previously published in Meyer et al. (2011) and $\delta^{44/40}$Ca data includes values from Payne et al. (2010; open squares). Open gray points are dolomitized and excluded from the smoothing curve, and sequence boundaries are identified as "SB".

Figure 3: Taşkent stratigraphic section showing δ^{13}C data relative to VPDB and $\delta^{44/40}$Ca data relative to BSE and SRM-915a. Smoothing curve and confidence interval are produced using a spline smoothing fit and a Monte Carlo procedure. $\delta^{44/40}$Ca error bars are 2σ from multiple analyses of the same sample. δ^{13}C data were previously published in Lau et al. (2016). Open gray points are dolomitized and excluded from the smoothing curve, and sequence boundaries are identified as "SB".

Figure 4: Combined δ^{13}C and $\delta^{44/40}$Ca from Dajiang (red circles) and Taşkent (blue triangles) from (A) the Late Permian to Late Triassic and (B) Early Triassic only (within the dashed lines in A). Smoothing curve and confidence interval are produced using a spline fit and a Monte Carlo procedure that incorporates the variability from error on the measurements. Gray, open points are dolomitized and excluded from the smoothing curve.

Figure 5: Combined δ^{13}C, $\delta^{44/40}$Ca, δ^{18}O, Mg/Ca, Mn/Sr, [Sr], and [Mn] data from Dajiang (red circles) and Taşkent (blue triangles) from the (A) Late Permian to Late Triassic and (B) Early Triassic only. Gray points are dolomitized. Ratios are mg kg^{-1} / mg kg^{-1}. Note log scale for [Sr] and [Mn].

Figure 6: Scatterplots of $\delta^{44/40}$Ca vs. other geochemical data. Open circles are from Dajiang and open triangles are from Taşkent. Colors represent different carbonate rock fabric types as indicated in the legend. Note log axes.

Figure 7: Conceptual model depicting the relationship between $\delta^{44/40}$Ca and [Sr] for seawater and carbonates for scenarios of: (A) mass flux imbalances in the seawater Ca and Sr cycles; (B) variations in the kinetic fractionation factor from a change in precipitation rate; (C) linear mixing between $CaCO_3$ polymorph end-members with distinct fractionation factors; and (D) post-

deposition alteration from linear mixing with Sr-depleted submarine groundwaters, Sr-enriched burial brines, or diagenetic resetting with seawater. These factors are not mutually exclusive: for example, an acidification event would include both reduced $CaCO_3$ burial (panel A) and a smaller fractionation factor (panel B) that may counteract their effects on bulk carbonate $\delta^{44/40}$Ca.

Figure 8: Scatterplots of (A) $\delta^{44/40}$Ca and [Sr] on a linear scale, (B) $\delta^{44/40}$Ca and [Sr] on a log scale, (C) $\delta^{44/40}$Ca and Sr/Ca on a linear scale, and (D) $\delta^{44/40}$Ca and Sr/Ca on a log scale for Dajiang (red circles) and Taşkent (blue triangles). A log-linear SMA model that describes the correlation in (B) is statistically better than the linear SMA model in (A) (ΔAIC=-1902).

Figure 9: Evolution of (A) δ^{18}O, (B) δ^{13}C, (C) $\delta^{44/40}$Ca, and (D) [Sr] in carbonate sediments interacting with seawater using a water-rock interaction model modified from Banner and Hanson (1990). As *N* increases, a greater volume of water has passed through the modeled system. In (C) and (D), the evolution for sediments that are originally 50% calcitic and 50% aragonitic are plotted against the left-hand y-axis and the evolution for sediments that are originally 100% aragonitic are plotted against the right-hand y-axis. Assumed fluid and solid compositions are shown, and porosity is set at 40% with a rock density of 3 g/mL. Crossplot of modeled $\delta^{44/40}$Ca and [Sr] overlain over data from Dajiang (circles) and Taskent (triangles), with arrows showing the path of recrystallization to calcite along (E) a linear [Sr] axis and (F) a logarithmic [Sr] axis. The recrystallization path for five initial aragonite-calcite mixtures are shown.

Figure 10: Boxplots of $\delta^{44/40}$Ca and [Sr] grouped by carbonate fabric type for Dajiang (left, red) and Taşkent (right, blue). Boxes are defined by the median, first quartile, and third quartile of the data, and the whiskers denote the interquartile range. $\delta^{44/40}$Ca for Dajiang differ statistically depending on fabric type (Table 5), whereas $\delta^{44/40}$Ca for Taskent do not. Grain-supported fabric types include grainstones, packstones, and oolites, and matrix-supported fabric types include wackestones and mudstones. The number of samples within each fabric type are shown below each boxplot in parentheses.

Figure 11: Scatterplots of $\delta^{44/40}$Ca compared to (A, B) [Sr], (C, D) Sr/Ca, and (E, F) Sr/(Ca+Mg) compiled from previously published studies. Left panels are plotted on a linear scale and right panels are plotted on a logarithmic scale. Red circles are data from this study, whereas open symbols are from studies in carbonate rocks and blue triangles are data from shallow marine carbonate sediments. Data plotted from Silva-Tamayo et al. (in review) are from Oman and Italy. The standardized major axis regression for datasets that exhibit a statistically significant correlation are plotted, depending on whether the linear or log-linear models were a better fit.

Figure 12: Comparison of the intercept of log-linear regressions with inferred seawater $\delta^{44/40}$Ca through the Phanerozoic. (A) The intercepts from Table A.1 for datasets that have statistically significant log-linear relationships between [Sr] and $\delta^{44/40}$Ca are plotted at the approximate

midpoint of the dataset, with horizontal error bars showing the approximate range. Vertical error bars are 1 SE. (1) Sawaki et al. (2014), (2) Husson et al. (2015), (3) Holmden et al. (2012a), (4) this study, and (5) Jost et al. (2017). Intercepts for Holmden (2009) and Farkaš et al. (2016) are not plotted because these datasets are primarily driven by dolomitization and kinetic reaction rates, respectively. (B) Reconstruction of seawater $\delta^{44/40}$Ca across the Phanerozoic, compiled by Blättler et al. (2012; see references therein). Temporal ranges of inferred aragonite and calcite seas are from Stanley (2006).

Figure 1

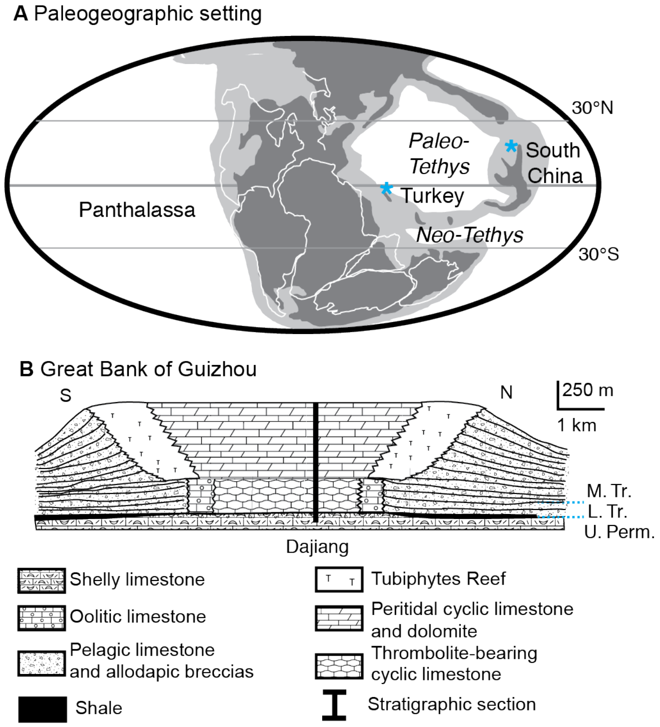

Figure 2

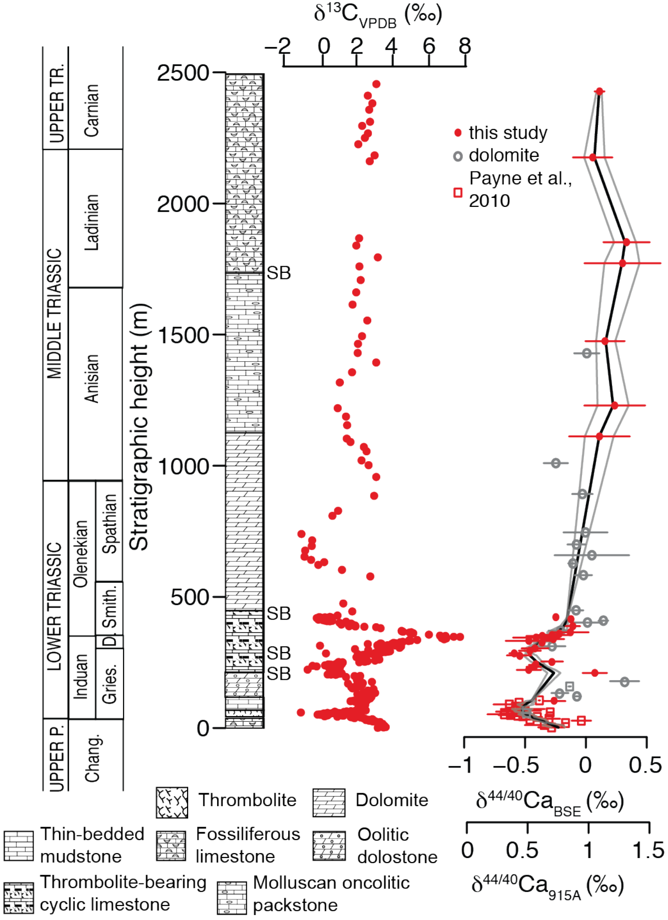

δ13CVPDB (‰)
−2
0
2
4
6
8
2500
2000
1500
1000
500
0
Stratigraphic height (m)
UPPER TR.
Carnian
MIDDLE TRIASSIC
Ladinian
Anisian
LOWER TRIASSIC
Olenekian
Spathian
Smith.
D.
Induan
Gries.
UPPER P.
Chang.
SB
SB
SB
SB
this study
dolomite
Payne et al., 2010
−1
−0.5
0
0.5
δ44/40CaBSE (‰)
0
0.5
1
1.5
δ44/40Ca915A (‰)
Thrombolite
Dolomite
Thin-bedded mudstone
Fossiliferous limestone
Oolitic dolostone
Thrombolite-bearing cyclic limestone
Molluscan oncolitic packstone

Figure 3

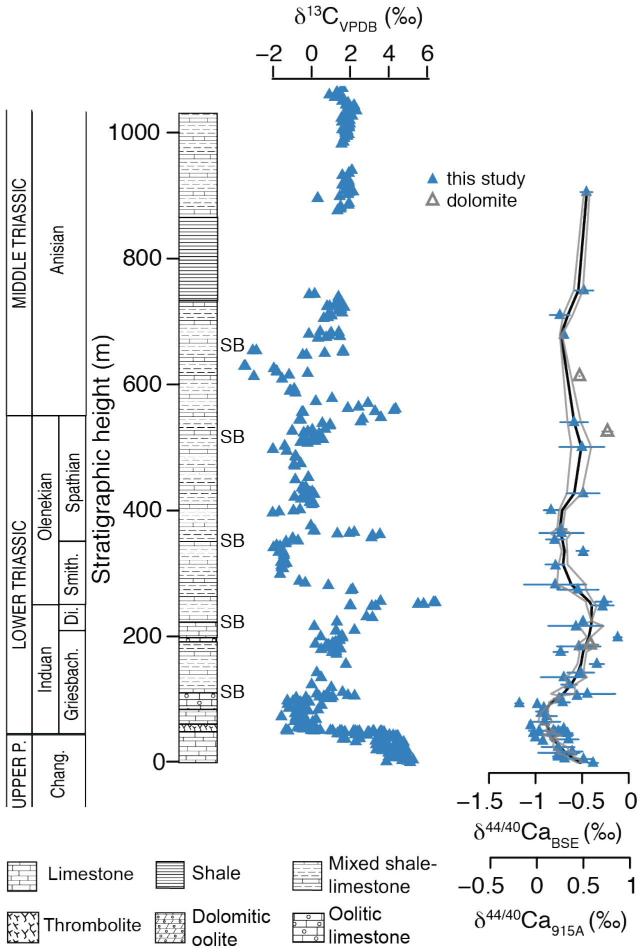

Figure 4

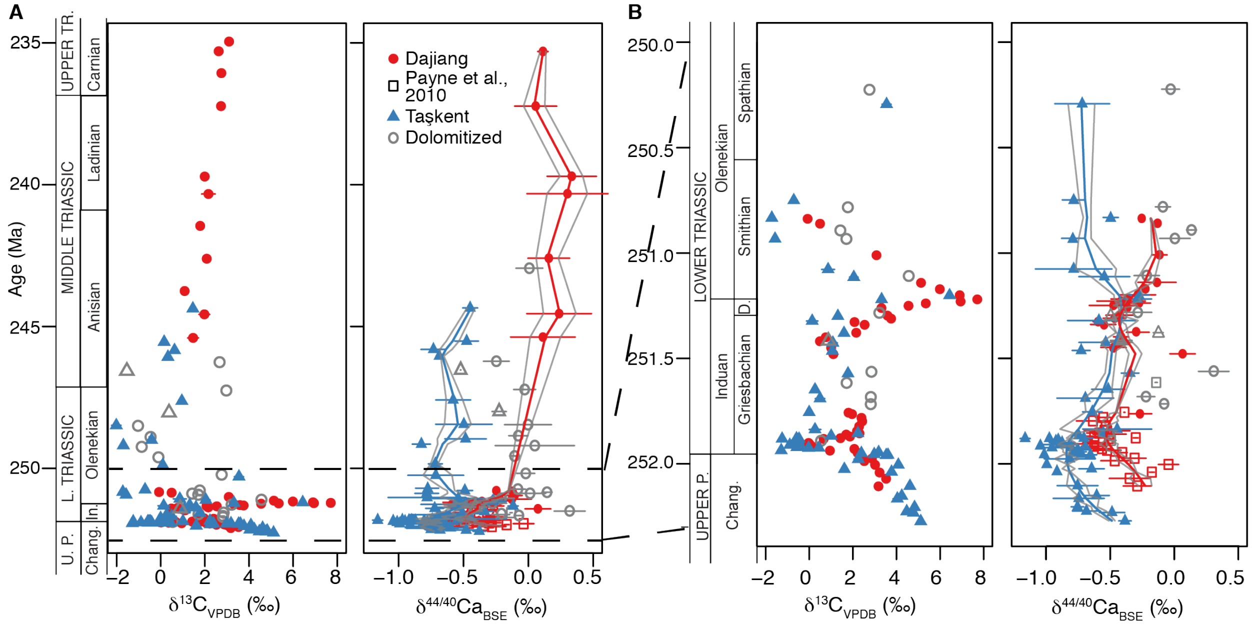

Figure 5

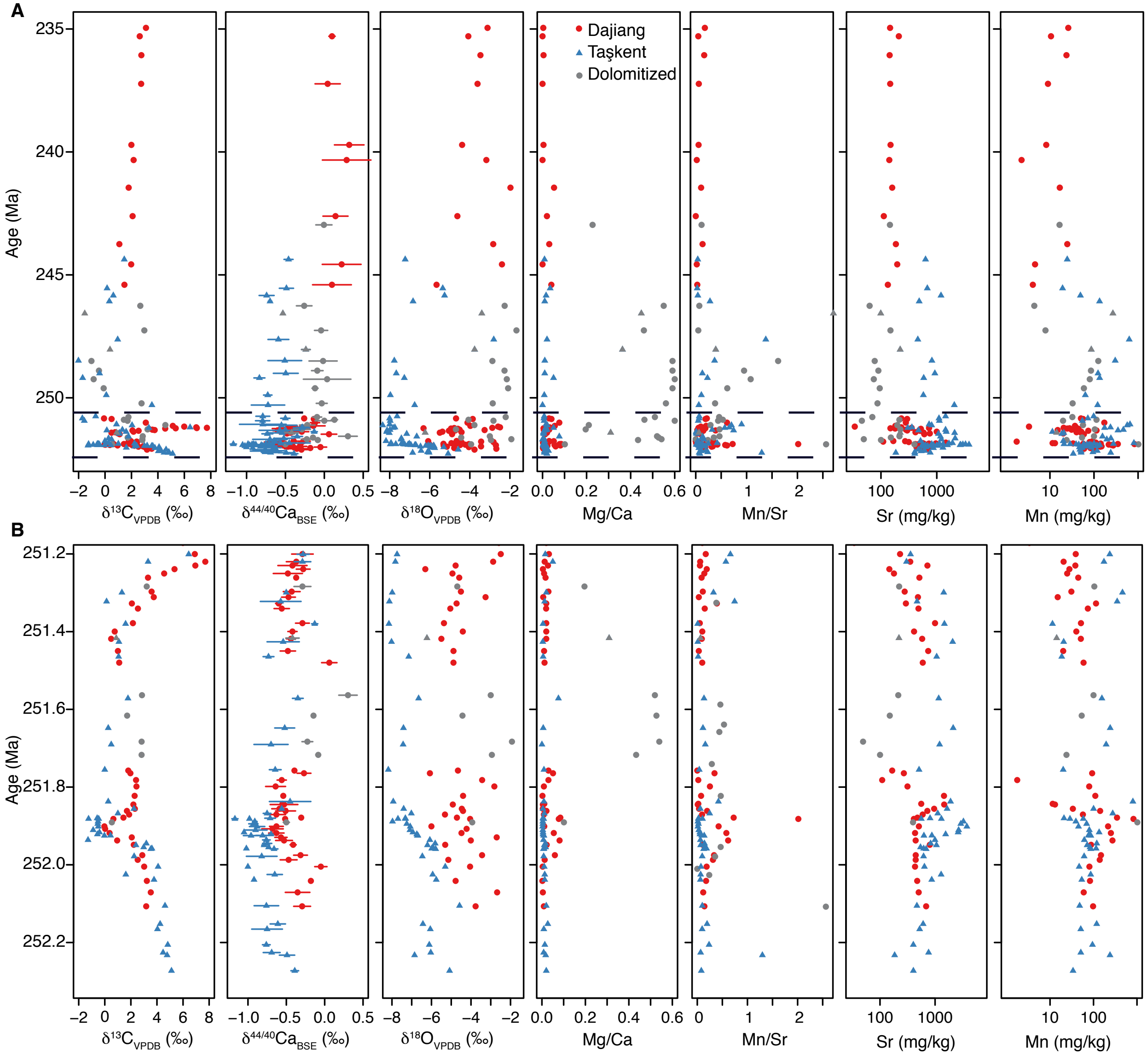
A
B
Age (Ma)
235
240
245
250
251.2
251.4
251.6
251.8
252.0
252.2
Dajiang
Taşkent
Dolomitized
−2 0 2 4 6 8
$\delta^{13}C_{VPDB}$ (‰)
−1.0 −0.5 0.0 0.5
$\delta^{44/40}Ca_{BSE}$ (‰)
−8 −6 −4 −2
$\delta^{18}O_{VPDB}$ (‰)
0.0 0.2 0.4 0.6
Mg/Ca
0 1 2
Mn/Sr
100 1000
Sr (mg/kg)
10 100
Mn (mg/kg)

Figure 6

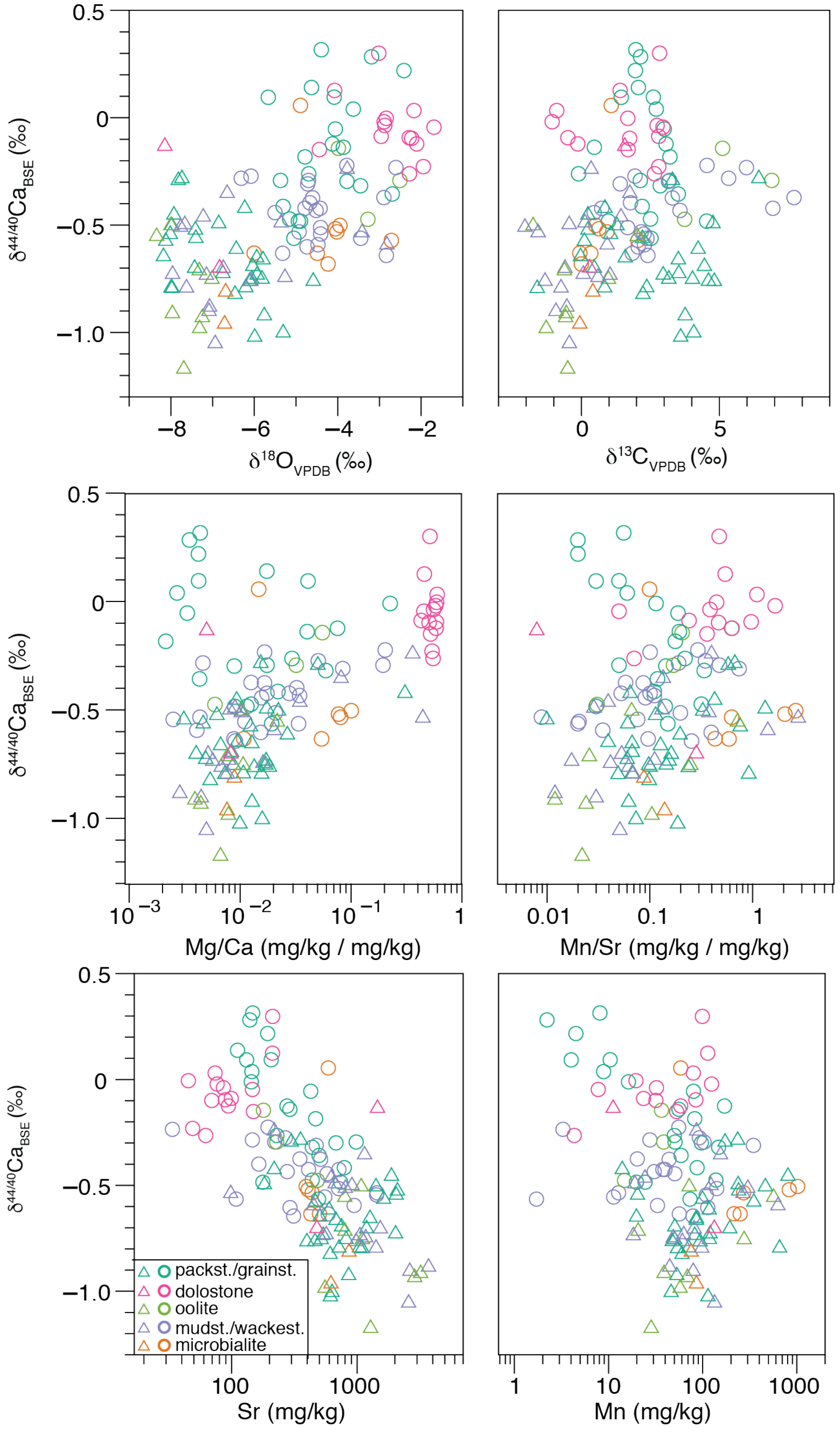
0.5
0
−0.5
−1.0
$\delta^{44/40}Ca_{BSE}$ (‰)
−8
−6
−4
−2
$\delta^{18}O_{VPDB}$ (‰)
0
5
$\delta^{13}C_{VPDB}$ (‰)
10^{-3}
10^{-2}
10^{-1}
1
Mg/Ca (mg/kg / mg/kg)
0.01
0.1
1
Mn/Sr (mg/kg / mg/kg)
△ ○ packst./grainst.
△ ○ dolostone
△ ○ oolite
△ ○ mudst./wackest.
△ ○ microbialite
100
1000
Sr (mg/kg)
1
10
100
1000
Mn (mg/kg)

Figure 7

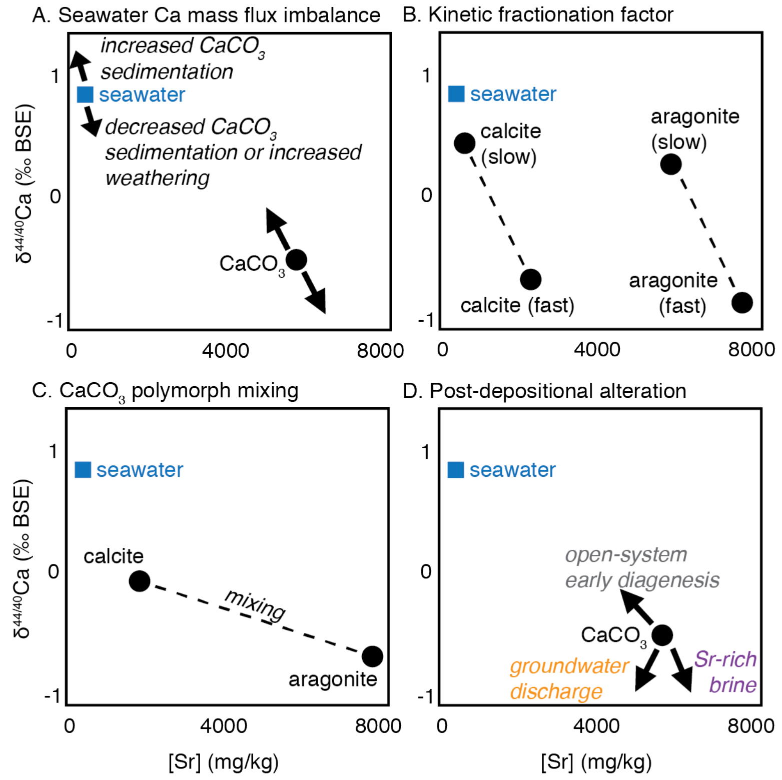

Figure 8

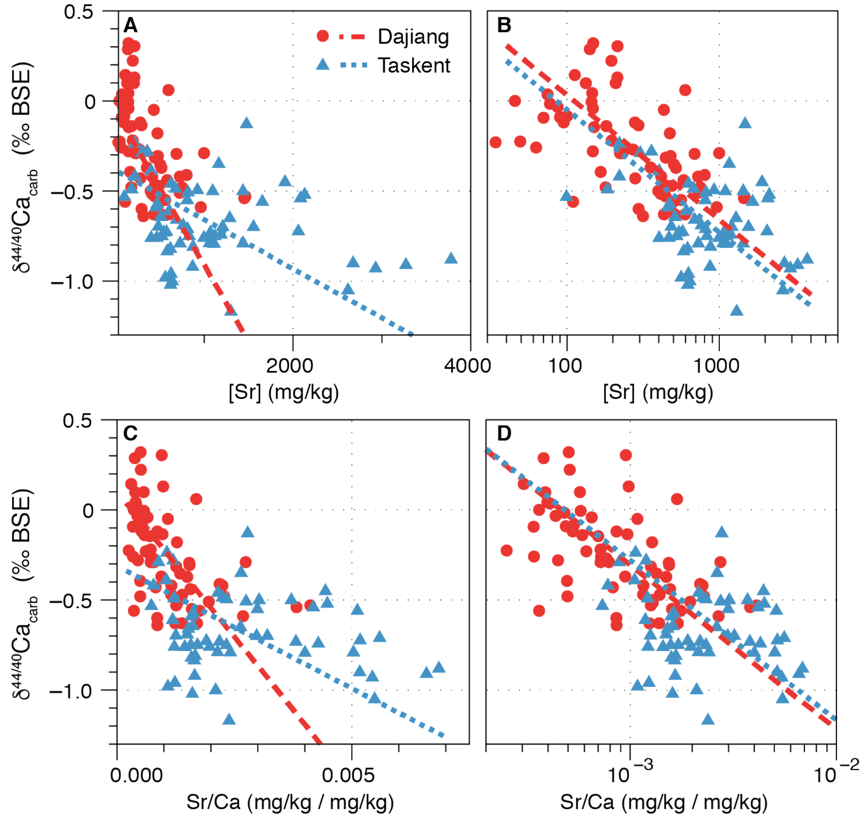

Figure 9

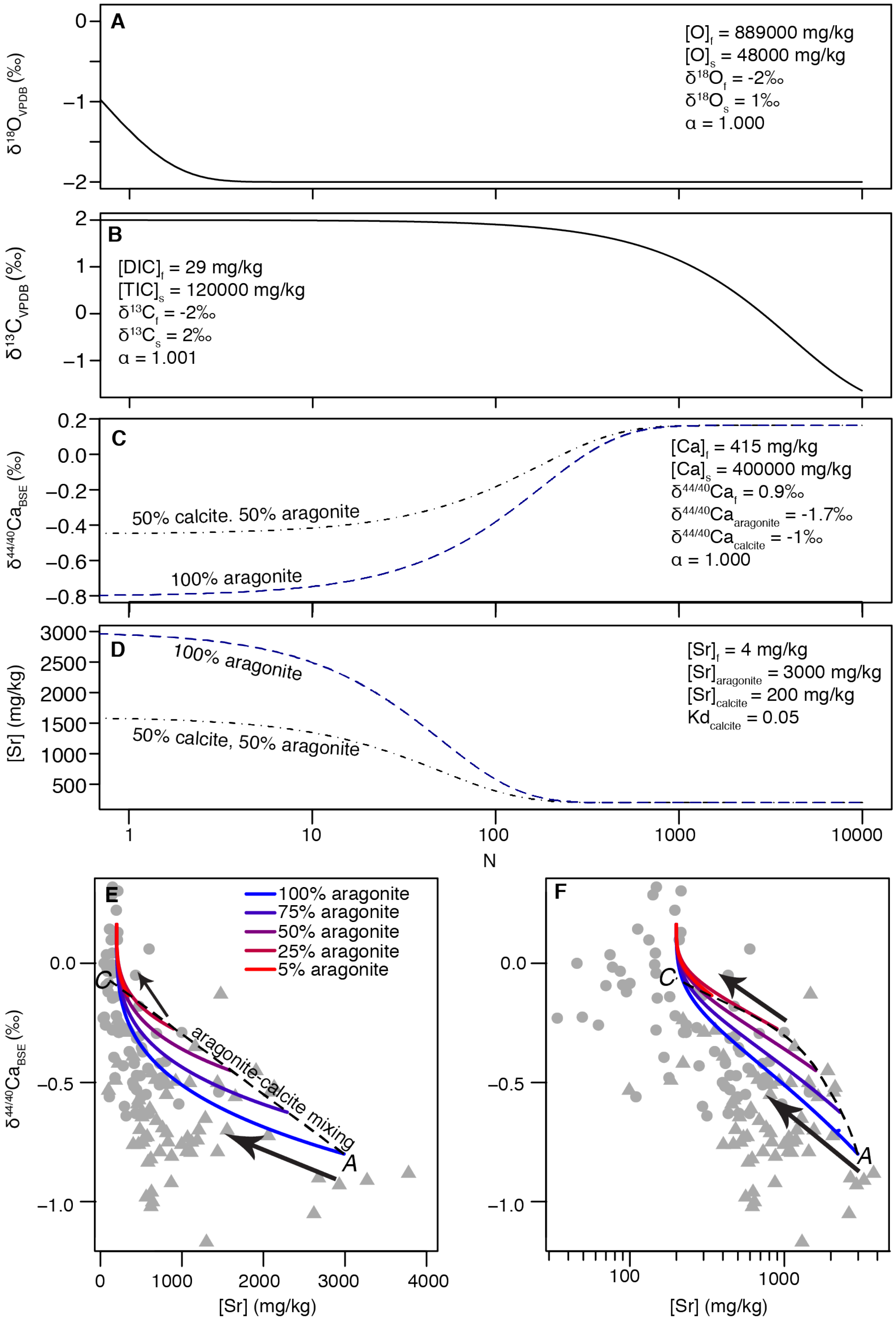
A
[O]$_f$ = 889000 mg/kg
[O]$_s$ = 48000 mg/kg
δ^{18}O$_f$ = -2‰
δ^{18}O$_s$ = 1‰
α = 1.000
δ^{18}O$_{VPDB}$ (‰)
0
−1
−2
B
[DIC]$_f$ = 29 mg/kg
[TIC]$_s$ = 120000 mg/kg
δ^{13}C$_f$ = -2‰
δ^{13}C$_s$ = 2‰
α = 1.001
δ^{13}C$_{VPDB}$ (‰)
2
1
0
−1
C
50% calcite. 50% aragonite
100% aragonite
[Ca]$_f$ = 415 mg/kg
[Ca]$_s$ = 400000 mg/kg
δ$^{44/40}$Ca$_f$ = 0.9‰
δ$^{44/40}$Ca$_{aragonite}$ = -1.7‰
δ$^{44/40}$Ca$_{calcite}$ = -1‰
α = 1.000
δ$^{44/40}$Ca$_{BSE}$ (‰)
0.2
0.0
−0.2
−0.4
−0.6
−0.8
D
100% aragonite
50% calcite, 50% aragonite
[Sr]$_f$ = 4 mg/kg
[Sr]$_{aragonite}$ = 3000 mg/kg
[Sr]$_{calcite}$ = 200 mg/kg
Kd$_{calcite}$ = 0.05
[Sr] (mg/kg)
3000
2500
2000
1500
1000
500
1
10
100
1000
10000
N
E
100% aragonite
75% aragonite
50% aragonite
25% aragonite
5% aragonite
C
aragonite-calcite mixing
A
δ$^{44/40}$Ca$_{BSE}$ (‰)
0.0
−0.5
−1.0
0
1000
2000
3000
4000
[Sr] (mg/kg)
F
C
A
0.0
−0.5
−1.0
100
1000
[Sr] (mg/kg)

1362 Figure 10

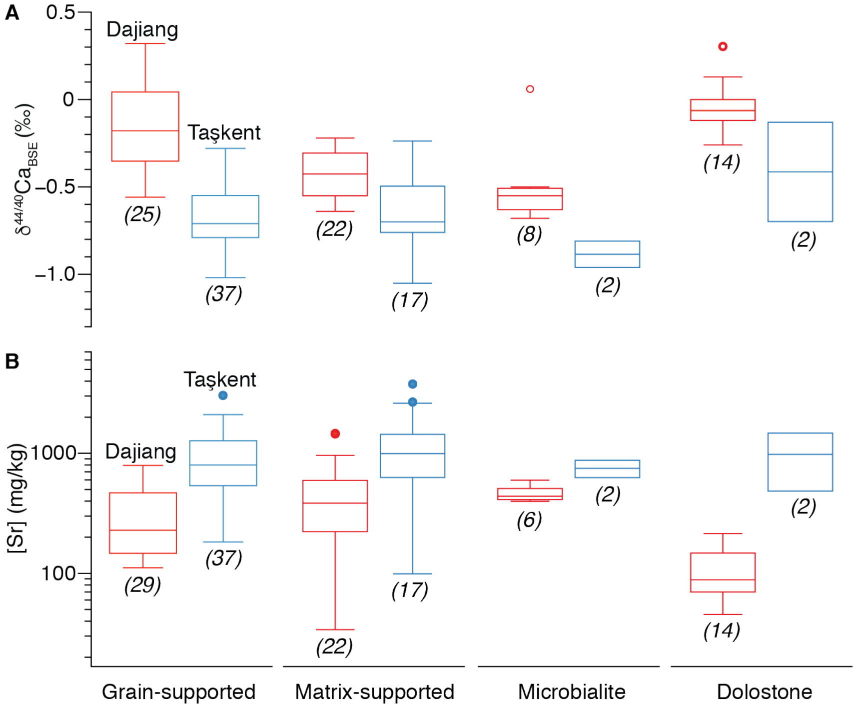

1363
1364

Figure 11

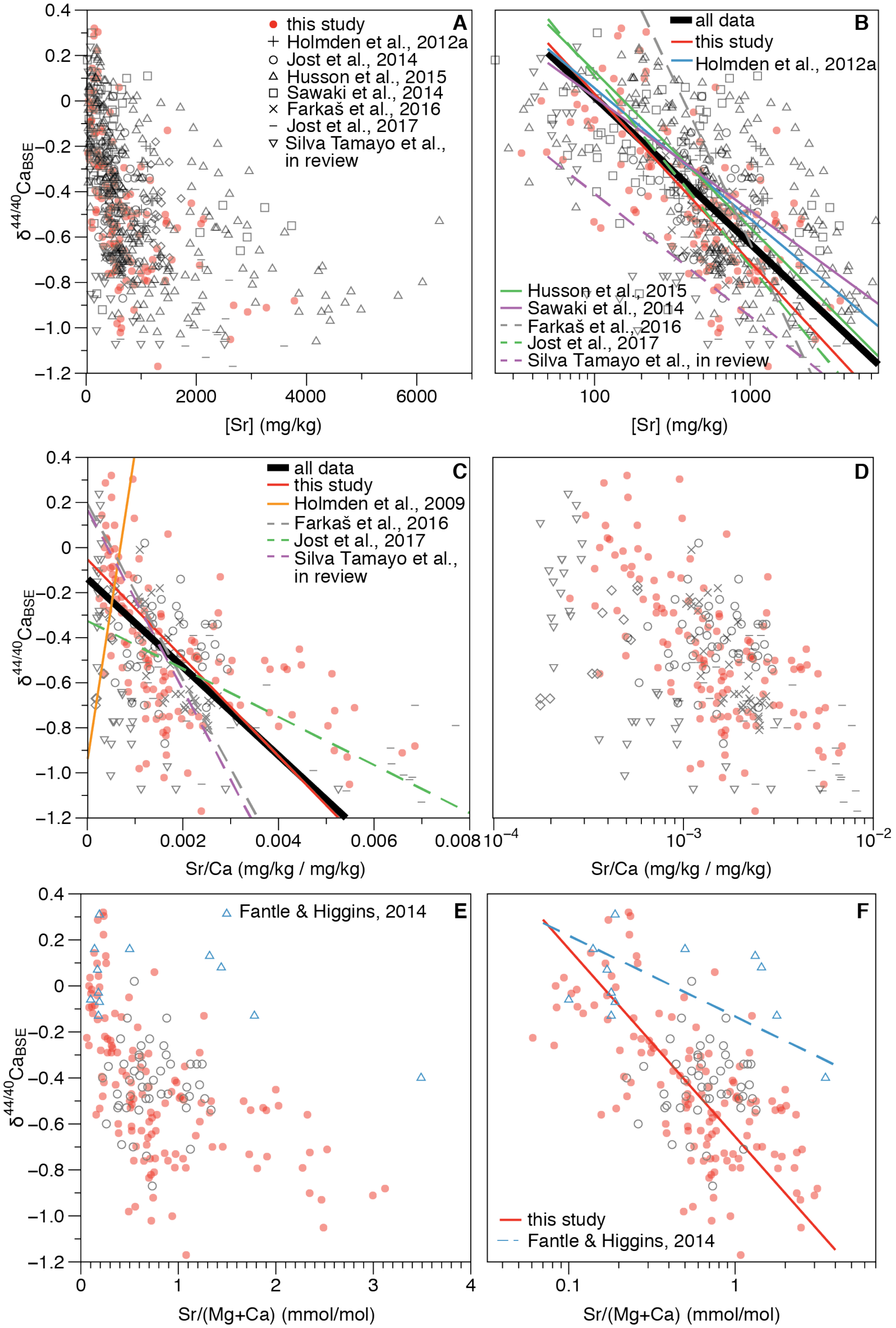
A
this study
Holmden et al., 2012a
Jost et al., 2014
Husson et al., 2015
Sawaki et al., 2014
Farkaš et al., 2016
Jost et al., 2017
Silva Tamayo et al., in review
$\delta^{44/40}Ca_{BSE}$
0.4
0.2
0
−0.2
−0.4
−0.6
−0.8
−1.0
−1.2
0
2000
4000
6000
[Sr] (mg/kg)
B
all data
this study
Holmden et al., 2012a
Husson et al., 2015
Sawaki et al., 2014
Farkaš et al., 2016
Jost et al., 2017
Silva Tamayo et al., in review
100
1000
[Sr] (mg/kg)
C
all data
this study
Holmden et al., 2009
Farkaš et al., 2016
Jost et al., 2017
Silva Tamayo et al., in review
0
0.002
0.004
0.006
0.008
Sr/Ca (mg/kg / mg/kg)
D
10^{-4}
10^{-3}
10^{-2}
Sr/Ca (mg/kg / mg/kg)
E
Fantle & Higgins, 2014
0
1
2
3
4
Sr/(Mg+Ca) (mmol/mol)
F
this study
Fantle & Higgins, 2014
0.1
1
Sr/(Mg+Ca) (mmol/mol)

Figure 12

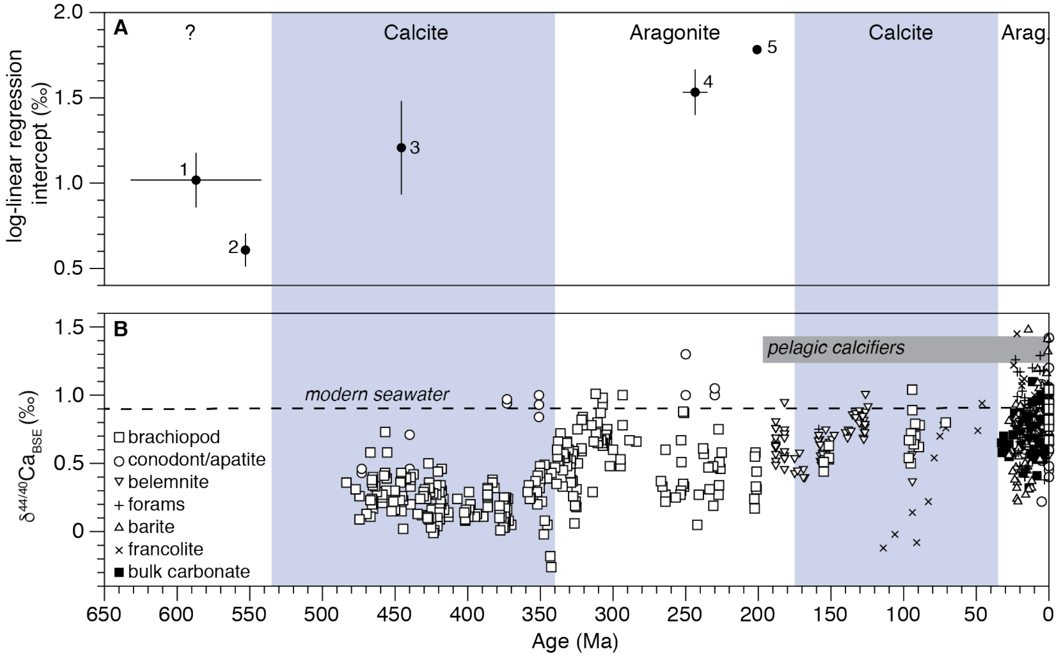
A
?
Calcite
Aragonite
Calcite
Arag.
1
2
3
4
5
log-linear regression intercept (‰)
2.0
1.5
1.0
0.5
B
pelagic calcifiers
modern seawater
$\delta^{44/40}Ca_{BSE}$ (‰)
1.5
1.0
0.5
0
□ brachiopod
○ conodont/apatite
▽ belemnite
+ forams
△ barite
× francolite
■ bulk carbonate
650
600
550
500
450
400
350
300
250
200
150
100
50
0
Age (Ma)

[Note: Tables 1 and S1 are submitted as separate, downloadable excel files]

Table 2: Spearman's ρ correlation statistics and R^2 values of $\delta^{44/40}$Ca with geochemical indicators for diagenesis (δ^{18}O, Mn/Sr, [Mn]), dolomitization (Mg/Ca, [Mg]), carbon cycling (δ^{13}C), and the strontium concentration ([Sr], log([Sr])). Mg/Ca* indicates the analysis was limited to samples with Mg/Ca < 0.1. Statistically significant correlations (α = 0.05) are bolded and italicized.

	Spearman's ρ	***p*-value**	**R^2**
	Dajiang		
$\delta^{18}O_{carb}$ (‰ VPDB)	***0.343***	***<0.01***	0.107
$\delta^{13}C_{carb}$ (‰ VPDB)	0.039	0.75	0.000
Mg/Ca	***0.273***	***0.03***	0.172
Mg/Ca*	-0.077	0.60	0.010
[Mg]*	-0.944	0.52	0.013
Mn/Sr	0.015	0.90	0.002
[Sr]	***-0.619***	***<0.001***	0.279
log([Sr])	***-0.619***	***<0.001***	0.312
[Mn]	***-0.313***	***0.01***	0.074
	Taşkent		
$\delta^{18}O_{carb}$ (‰ VPDB)	-0.133	0.31	0.000
$\delta^{13}C_{carb}$ (‰ VPDB)	0.197	0.13	0.031
Mg/Ca	***0.402***	***<0.01***	0.114
Mg/Ca*	***0.330***	***0.01***	0.128
[Mg]*	0.158	0.24	0.147
Mn/Sr	***0.281***	***0.03***	0.068
[Sr]	***-0.258***	***0.05***	0.084
log([Sr])	***-0.258***	***0.05***	0.110
[Mn]	0.189	0.15	0.050

Table 3: Summary of controls on the $\delta^{44/40}$Ca value of bulk carbonates.

Control	**References**	**Effect**	**Predicted Observation**
Early diagenesis	Fantle and DePaolo, 2007; Jacobson and Holmden, 2008; Griffith et al., 2015	At isotopic equilibrium, Δ_{c-s} = 0‰	Recrystallization with porewaters at equilibrium would produce positive offsets
	Teichert et al., 2009	Up to 0.8‰ negative shift observed in porewaters in silicilastic sediments (presumably less well-Ca-buffered than the carbonate sediment, possibly from Ca released from OM remineralization)	Assuming equilibrium, recrystallization would produce more muted positive offsets
Burial diagenesis	Amini et al., 2008	Hydrothermal fluids are ~0.95‰ more negative than seawater, but more positive relative to BSE	Assuming equilibrium, recrystallization would produce a small positive offset
	Teichert et al., 2009	Fluids that have interacted with oceanic basement are >1‰ more negative than seawater	Assuming equilibrium, recrystallization would produce more muted positive or minor negative offsets
Dolomitization	Heuser et al., 2005; Tipper et al., 2008; Holmden, 2009	Dolomitization occurs close to equilibrium; Δ_{c-s} = 0‰	Dependent on the $\delta^{44/40}$Ca of the dolomitizing fluid.
Submarine groundwater	Holmden et al., 2012b	Can mix with seawater to reduce $\delta^{44/40}$Ca by up to 1.2‰	Negative offset from primary values
Fractionation factor			
Precipitation rate	Lemarchand et al., 2004; Gussone et al., 2005; AlKhatib & Eisenhauer, 2017a,b	Negative correlation between precipitation rates and magnitude of Δ_{c-s}	Smaller fractionation (more positive values) with higher Sr
	Tang et al., 2008a; DePaolo, 2011; Nielsen et al., 2012; Watkins et al., 2017	Positive correlation between precipitation rates and magnitude of Δ_{c-s}	Larger fractionation (more negative values) with higher Sr
Temperature	Marriott et al., 2004; Griffith et al., 2008; Hippler et al., 2009; cf. Sime et al., 2005	Weak, positive correlation between temperature and magnitude of Δ_{c-s}	0.013 to 0.2‰ per °C
Carbonate mineralogy	Gussone et al., 2005; Blättler et al., 2012	Calcite Δ ~ -1.0 to -1.4‰; Aragonite Δ ~ -1.9‰	Larger fractionation (more negative values) with higher Sr
Biological control/vital effects	Skulan et al., 1997; Gothmann et al., 2016; Gussone et al., 2005; Steuber and Buhl, 2006	Inorganic calcite has a smaller Δ_{c-s} than organic calcite, but no observed difference for aragonite	More precipitation of inorganic calcite would result in more positive values
	Bohm et al., 2006; summarized in Farkaš et al., 2007; Blättler et al., 2012	Modern carbonates show a range of Δ_{c-s} values depending on mineralogy, where aragonite $\delta^{44/40}$Ca ~ -1.5‰, simple calcifiers $\delta^{44/40}$Ca ~-0.9‰, sophisticated calcifiers $\delta^{44/40}$Ca ~-1.3‰	Aragonitic carbonates would have more negative values than calcitic carbonates

Table 4: Parameters used in diagenetic water-rock interaction model (Figure 9).

Parameter	Definition	Value					
P	porosity	40 %					
ρ_f	fluid density	1 g/mL					
ρ_s	solid density	3 g/mL					
		O	C	Sr-calcite	Sr-aragonite	Ca-calcite	Ca-aragonite
$C_{f,o}$	initial fluid concentration (seawater)	889000 mg/kg[1]	29 mg/kg[1]	4 mg/kg[2]	4 mg/kg[2]	415 mg/kg[1]	415 mg/kg[1]
$C_{s,o}$	initial solid concentration	480000 mg/kg[1]	120000 mg/kg[1]	200 mg/kg[3]	3000 mg/kg[3]	400000 mg/kg[1]	400000 mg/kg[1]
D	single element distribution coefficient	0.54	4137.93	50	750	963.86	963.86
K_d	exchange reaction distribution coefficient	0.00056	4.29	0.052	0.778	1	1
$\delta I_{f,o}$	initial fluid isotopic value	-2[4]	-2[4]	NA	NA	0.9[5]	0.9[5]
$\delta I_{s,o}$	initial solid isotopic value	1[6]	2[6]	NA	NA	-1	-1.7
α	fractionation factor	1.000[7]	1.001[7]	NA	NA	1.000[8]	1.000[8]

[1] Banner and Hanson (1990)

[2] Half of value from Banner and Hanson (1990)

[3] estimates from modern carbonates (Kinsman 1969)

[4] early diagenetic fluids are typical more negative than primary carbonates (*e.g.*, Tucker and Wright, 1990)

[5] seawater value (Fantle and Tipper, 2015)

[6] Selected to represent typical recent carbonate values (Veizer et al., 1999)

[7] typical fractionation factor at 20 °C (*e.g.*, Tucker and Wright 1990)

[8] fractionation at equilibrium (Fantle and DePaolo, 2007)

Table 5: Tukey-Kramer pair-wise comparison for Dajiang $\delta^{44/40}Ca$, grouped by carbonate fabric type. Significant relationships ($\alpha = 0.05$) are bolded and italicized. ANOVA results indicate fabric type is not a statistically significant control for Taşkent. Matrix-supported fabric types include mudstones and wackestones, and grain-supported fabric types include packstones, grainstones, and oolites.

Fabric type A	**Fabric type B**	**Diff**	**Lower CI**	**Upper CI**	***p*-value**
Matrix-supported	Dolostone	***-0.39***	***-0.57***	***-0.28***	***<0.001***
Grain-supported	Dolostone	-0.12	-0.30	0.60	0.31
Microbialite	Dolostone	***-0.45***	***-0.69***	***-0.22***	***<0.001***
Grain-supported	Matrix-supported	***0.27***	***0.12***	***0.43***	***<0.001***
Microbialite	Matrix-supported	-0.06	-0.28	0.16	0.87
Microbialite	Grain-supported	***-0.34***	***-0.55***	***-0.12***	***<0.001***

Table 6: Thin-section estimates of microfacies contribution (by area).

Sample	Sparry calcite	Micrite	Micritic clasts	Recrystallized clasts	Peloids	Microcrystalline cement	Ooids	Skeletal
Dajiang								
PDJ-033	67	0	5	10	0	0	0	18
PDJ-040	0	0	10	0	0	78	0	12
PDJ-055	0	0	0	0	0	99	0	1
PDJ-058	0	10	0	0	0	80	0	10
PDJ-061	0	8	0	0	0	90	0	2
PDJ-064	0	0	0	4	0	95	0	1
PDJ-072	0	100	0	0	0	0	0	0
PDJ-075	0	85	0	0	0	15	0	0
PDJ-107	0	100	0	0	0	0	0	0
PDJ-115	0	100	0	0	0	0	0	0
PDJ-118	0	70	0	0	0	30	0	0
PDJ-127	100	0	0	0	0	0	0	0
PDJ-162	50	45	0	0	0	0	0	5
PDJ-216	0	98	0	0	0	0	0	2
PDJ-235	0	0	0	40	0	60	0	0
PDJ-247	0	100	0	0	0	0	0	0
PDJ-271	0	50	0	0	0	50	0	0
PDJ-274	0	60	0	40	0	0	0	0
PDJ-290	0	72	0	20	0	0	0	8
PDJ-299	0	70	0	10	0	20	0	0
PDJ-316	0	40	0	20	0	40	0	0
MDJ-31	0	80	0	0	0	20	0	0
Taşkent								
TCX-47	0	70	5	0	0	0	0	25
TK-0.03	0	67	10	10	0	0	0	13
TK-2.9	0	50	0	50	0	0	0	0
TK-27.1	25	0	0	0	0	0	75	0
TK-45.5	0	95	0	0	0	5	0	0
TK-76.5	5	10	40	0	0	45	0	0
TK-234	10	0	0	0	0	70	0	20
TK-450.5	3	0	15	0	75	0	0	7
TK-489.5	0	99	0	0	0	1	0	0
TKU-63.7	5	0	95	0	0	0	0	0

APPENDIX A

Carbonate diagenetic model

To illustrate the impact of diagenesis on Ca relative to other major and minor components of carbonates, we develop an open-system water-rock interaction model presented in Figure 9. In this set of calculations, we track the evolution of δ^{18}O, δ^{13}C, [Sr], and $\delta^{44/40}$Ca in a carbonate rock reacting with a fluid similar to seawater in order to determine the relative susceptibility of each of these components to alteration during early diagenesis. Following Banner and Hanson (1990), we calculate the concentration of each element in the fluid-rock system as

$$C_o = F \times C_{f,o} + \left(1-F\right) \times C_{s,o} \tag{A.1}$$

where C_o is the concentration of the element in the system, $C_{f,o}$ is the concentration of element I in the initial fluid, $C_{s,o}$ is the concentration of the element in the initial solid, and F is the weight fraction of the fluid as defined by

$$F = \frac{P \times \rho_f}{P \times \rho_f + \left(1-P\right)\rho_s} \tag{A.2}$$

where P is the porosity and ρ_s and ρ_f are the density of the solid and fluid, respectively. Given a distribution coefficient D, defined as C_s/C_f, the concentration of the element in the solid, C_s, at equilibrium is calculated by

$$C_s = \frac{C_o}{F/D + \left(1-F\right)} \quad \text{(A.3).}$$

The isotopic composition of element I in the solid, expressed in delta notation as δI_s, can also be tracked using the following equation:

$$\delta I_s = \frac{\delta I_o C_o \alpha - 1000 C_f F\left(1-\alpha\right)}{C_s\left(1-F\right)\alpha + C_f F} \tag{A.4}$$

where δI_o is the isotopic composition of the water-rock system and α is the fractionation factor between the fluid and the solid. The degree of water-rock interaction is represented by N:

$$N = n \times \left(F/\left(1-F\right)\right) \tag{A.5}$$

where n is the number of iterations.

We assume that the distribution coefficients (D), fractionation factors (α), and initial fluid and solid compositions (C) are similar to those of modern marine carbonate sediments as described in Table 4, and that these did not vary through time or with biotic versus abiotic precipitation.

Reference

Banner, J.L., Hanson, G.N., 1990. Calculation of simultaneous isotopic and trace element variations during water-rock interaction with applications to carbonate diagenesis. Geochimica et Cosmochimica Acta 54, 3123-3137.

Table 1. Isotopic and geochemical data.

Sample	**Stratigraphic height (m)**	**Age (yr)**	**Lithology**[1]	**$\delta^{13}C_{carb}$ (‰VPDB)**	**$\delta^{18}O_{carb}$ (‰VPDB)**	**$\delta^{44/40}Ca_{carb}$ (‰BSE)**	**$\delta^{44/40}Ca_{carb}$ (‰915a)**	**2σ (‰)**	**n**	**Lab**	**Mg/Ca**	**Mn/Sr**	**Sr/Ca**	**Mn (ppm)**	**Sr (ppm)**	**Reference**
							Dajiang									
PDJ-001	0	252.107	PG	3.18	-3.77	-0.29	0.71	0.11	3	Berkeley	0.009	0.142	0.0015	97.7	687.9	Payne et al., 2010
PDJ-009	9	252.071	PG	3.53	-2.68	-0.35	0.65	0.16	2	Berkeley	0.004	0.118	0.0013	59.5	504.0	Payne et al., 2010
PDJ-017	16.4	252.041	PG	3.23	-4.78	-0.18	0.82	0.02	2	Berkeley	0.002	0.175	0.0013	83.0	473.5	Payne et al., 2010
PDJ-026	25.6	252.005	PG	3.02	-4.05	-0.05	0.95	0.08	2	Berkeley	0.003	0.186	0.0011	80.5	432.5	Payne et al., 2010
PDJ-030	30	251.987	PG	2.52	-5.15	-0.47	0.53	0.11	2	Berkeley	0.013	0.313	0.0012	139.0	444.5	Payne et al., 2010
PDJ-033	33	251.975	PG	2.88	-3.44	-0.31	0.69	0.09	3	Berkeley	0.060	0.334	0.0013	148.5	445.0	Payne et al., 2010
PDJ-040	39.7	251.949	PG	2.22	-5.31	-0.41	0.59	0.04	1	Berkeley	0.022	0.110	0.0022	88.0	802.0	Payne et al., 2010
PDJ-044	42.5	251.937	TH	0.95	-4.01	-0.53	0.47	0.11	2	Berkeley	0.081	0.615	0.0013	273.0	444.0	Payne et al., 2010
PDJ-046	44.5	251.929	TH	2.07	-2.70	-0.57	0.43	0.08	2	Berkeley	--	--	--	--	--	Payne et al., 2010
PDJ-050	47.3	251.918	TH	0.37	-4.48	-0.63	0.37	0.10	1	Berkeley	0.055	0.580	0.0012	251.0	433.0	Payne et al., 2010
PDJ-053	50	251.908	TH	0.03	-4.22	-0.68	0.32	0.14	3	Berkeley	--	--	--	--	--	Payne et al., 2010
PDJ-055	51.6	251.901	TH	-0.03	-6.00	-0.63	0.37	0.09	2	Berkeley	0.011	0.425	0.0014	216.0	508.0	Payne et al., 2010
PDJ-058	54.2	251.891	TH	0.54	-3.94	-0.50	0.50	0.04	2	Berkeley	0.101	2.564	0.0013	1019.0	397.5	Payne et al., 2010
PDJ-061	56.4	251.882	TH	0.66	-4.04	-0.52	0.48	0.01	2	Berkeley	0.078	2.015	0.0013	830.0	412.0	Payne et al., 2010
PDJ-064	57.4	251.879	MW	1.43	-4.71	-0.31	0.69	0.02	2	Berkeley	0.085	0.725	0.0015	347.0	478.5	Payne et al., 2010
PDJ-068	60.4	251.871	MW	1.87	-5.32	-0.63	0.37	0.12	2	Berkeley	0.009	0.096	0.0017	57.0	595.5	Payne et al., 2010
PDJ-072	63.9	251.861	MW	1.70	-4.40	-0.51	0.49	0.13	2	Berkeley	0.021	0.196	0.0020	142.0	724.0	Payne et al., 2010
PDJ-075	66	251.856	MW	2.31	-4.47	-0.59	0.41	0.10	1	Berkeley	0.004	0.035	0.0027	33.5	961.5	Payne et al., 2010
PDJ-080	70.1	251.845	MW	2.19	-4.92	-0.53	0.47	0.18	2	Berkeley	0.004	0.009	0.0041	13.0	1463.0	Payne et al., 2010
PDJ-081	70.7	251.843	MW	--	--	-0.55	0.45	--	3	Berkeley	0.011	0.021	0.0016	11.5	560.5	Payne et al., 2010
PDJ-090	77.6	251.823	MW	2.29	-4.40	-0.54	0.46	--	2	Berkeley	0.002	0.076	0.0038	110.0	1452	Payne et al., 2010
PDJ-100	87.6	251.798	MW	2.43	-2.82	-0.64	0.36	0.13	2	Berkeley	0.009	0.252	0.0009	79.5	315.5	Payne et al., 2010
PDJ-107	93.8	251.782	MW	2.40	-3.44	-0.56	0.44	0.06	2	Berkeley	0.034	0.020	0.0004	1.8	109.6	this study
PDJ-115	100.4	251.764	MW	1.96	-6.08	-0.27	0.73	0.09	2	Berkeley	0.051	0.343	0.0008	93.0	271.0	Payne et al., 2010
PDJ-118	103	251.758	MW	1.80	-4.66	-0.39	0.61	0.01	2	Berkeley	0.033	0.000	0.0005	0.0	166.4	this study
PDJ-127	118.2	251.717	DL	2.82	-2.94	-0.08	0.92	0.03	2	Berkeley	0.433	0.238	0.0005	23.9	100.2	this study
PDJ-132	131	251.683	DL	2.82	-1.93	-0.23	0.77	0.07	2	Berkeley	0.543	0.000	0.0003	0.0	49.3	this study
PDJ-140	156.2	251.616	DL	1.71	-4.43	-0.15	0.85	0.01	2	Berkeley	0.527	0.355	0.0007	53.5	150.5	Payne et al., 2010
PDJ-148	176	251.564	DL	2.85	-3.00	0.30	1.30	0.12	4	Berkeley	0.520	0.466	0.0010	100.0	214.5	this study
PDJ-162	207.5	251.480	TH	1.11	-4.89	0.06	1.06	0.10	4	Berkeley	0.015	0.099	0.0017	59.0	597.5	this study
PDJ-171	218.8	251.450	PG	1.01	-4.89	-0.48	0.52	0.10	3	GEOMAR	0.012	0.030	0.0023	20.1	750.0	this study
PDJ-179	230.6	251.418	MW	0.49	-5.50	-0.44	0.56	0.06	3	GEOMAR	0.016	0.090	0.0016	51.1	582.8	this study
PDJ-191	237.75	251.400	MW	0.76	-4.41	-0.42	0.58	0.06	3	GEOMAR	0.018	0.100	0.0012	40.2	415.4	this study
PDJ-201	251	251.378	PG	2.16	-5.37	-0.29	0.71	0.09	3	GEOMAR	0.018	0.050	0.0027	51.4	997.8	this study
PDJ-216	274.1	251.341	PG	2.54	-5.05	-0.56	0.44	0.10	3	GEOMAR	0.019	0.148	0.0018	74.1	499.2	this study
PDJ-224	282.2	251.327	MW	2.08	-4.73	-0.60	0.40	0.04	3	GEOMAR	0.015	0.390	0.0009	114.1	295.2	this study
PDJ-235	292.2	251.311	OL	3.76	-3.26	-0.47	0.53	0.09	2	Berkeley	0.006	0.031	0.0014	15.0	488.5	this study
PDJ-241	301	251.297	MW	3.59	-4.51	-0.43	0.57	0.11	3	GEOMAR	0.035	0.110	0.0008	30.9	280.6	this study
PDJ-247	309.1	251.284	MW	3.22	-4.69	-0.29	0.71	0.11	3	GEOMAR	0.196	0.468	0.0008	104.3	222.6	this study
PDJ-260	323.1	251.261	MW	3.31	-4.60	-0.37	0.63	0.02	2	Berkeley	0.017	0.086	0.0015	44.5	519.0	this study
PDJ-265	329.7	251.250	PG	4.55	-4.94	-0.48	0.52	0.19	3	GEOMAR	0.009	0.140	0.0005	24.8	179.2	this study
PDJ-269	336.6	251.239	MW	5.35	-6.31	-0.28	0.72	0.09	3	GEOMAR	0.005	0.189	0.0004	27.9	147.8	this study
PDJ-271	342.3	251.230	MW	6.94	-4.78	-0.42	0.58	0.19	3	GEOMAR	0.028	0.053	0.0022	38.2	726.2	this study
PDJ-274	348.4	251.220	MW	7.71	-2.88	-0.37	0.63	0.13	3	GEOMAR	0.013	0.058	0.0009	20.5	354.0	this study
PDJ-276	351.9	251.200	OL	6.90	-2.49	-0.29	0.71	0.14	3	GEOMAR	0.032	0.169	0.0007	39.0	231.3	this study
PDJ-279	357	251.172	MW	5.99	-2.59	-0.23	0.77	0.02	3	GEOMAR	0.017	0.100	0.0006	3.3	33.9	this study
PDJ-282	362.4	251.141	OL	5.13	-3.97	-0.14	0.86	0.15	3	GEOMAR	0.056	0.204	0.0006	37.0	181.2	this study
PDJ-286	368.2	251.109	MW	4.56	-3.77	-0.22	0.78	0.10	3	GEOMAR	0.205	0.290	0.0007	56.3	196.6	this study
PDJ-290	385.7	251.011	PG	3.08	-4.12	-0.12	0.88	0.06	2	Berkeley	0.076	0.615	0.0009	171.5	279.0	this study
PDJ-299	399.5	250.933	DL	1.70	-2.82	0.00	1.00	0.12	3	GEOMAR	0.597	0.440	0.0004	19.8	45.5	this study
PDJ-301	406.7	250.893	DL	1.43	-4.07	0.13	1.13	0.04	2	Berkeley	0.462	0.533	0.0010	114.0	214.0	this study
PDJ-307	412.35	250.861	PG	0.50	-3.86	-0.14	0.86	0.02	2	Berkeley	0.040	0.192	0.0010	56.5	294.5	this study
PDJ-316	419.9	250.838	PG	-0.08	-4.69	-0.26	0.74	0.01	2	Berkeley	0.030	0.218	0.0007	50.5	232.0	this study
DJB-03	445.9	250.783	DL	1.77	-2.21	-0.09	0.91	0.06	2	Berkeley	0.511	0.460	0.0003	32.3	70.0	this study
DJB-06	579.9	250.225	DL	2.76	-2.86	-0.03	0.97	0.07	2	Berkeley	0.560	0.380	0.0004	32.7	86.7	this study
DJB-08	624.3	249.612	DL	-0.10	-2.09	-0.12	0.88	0.04	2	Berkeley	0.590	0.620	0.0005	59.0	95.0	this study
DJB-11	655.6	249.243	DL	-0.86	-2.15	0.04	1.04	0.31	2	Berkeley	0.604	1.080	0.0004	80.3	74.4	this study
DJB-13	696.5	248.895	DL	-0.46	-2.27	-0.09	0.91	0.07	2	Berkeley	0.594	0.950	0.0005	85.4	89.9	this study
DJB-15	742.6	248.503	DL	-1.03	-2.87	-0.02	0.88	0.18	2	Berkeley	0.586	1.620	0.0005	125.1	77.3	this study
DJB-19	888.8	247.258	DL	2.97	-1.67	-0.04	0.96	0.08	2	Berkeley	0.458	0.050	0.0007	7.9	147.9	this study
DJB-21	1006.3	246.259	DL	2.67	-2.26	-0.26	0.74	0.10	3	Berkeley	0.555	0.070	0.0003	4.4	62.6	this study
DJB-27	1108.1	245.403	PG	1.47	-5.66	0.10	1.00	0.25	2	Berkeley	0.041	0.030	0.0004	4.1	132.9	this study
MDJ-31	1226	244.573	PG	1.98	-2.40	0.22	1.12	0.25	3	Berkeley	0.004	0.020	0.0005	4.6	195.6	this study

DJB-46	1424.8	242.966	PG	--	--	-0.01	0.99	0.10	2	Berkeley	0.227	0.114	0.0006	16.5	144.8	this study
DJB-48	1470.9	242.612	PG	2.09	-4.62	0.14	1.04	0.16	3	Berkeley	0.017	0.000	0.0003	0.0	112.4	this study
DJB-57	1767.6	240.329	PG	2.16	-3.17	0.29	1.29	0.31	4	Berkeley	0.003	0.020	0.0004	2.3	141.0	this study
DJB-60	1847.7	239.713	PG	1.99	-4.38	0.32	1.32	0.19	3	Berkeley	0.004	0.056	0.0005	8.2	148.5	this study
DJB-62	2170.5	237.230	PG	2.73	-3.62	0.04	0.94	0.16	3	Berkeley	0.003	0.060	0.0004	9.0	146.4	this study
DJB-71	2422.0	235.296	PG	2.63	-4.08	0.10	1.10	0.04	2	Berkeley	0.004	0.050	0.0006	10.6	208.9	this study
							Taşkent									
TCX-0	0	252.273	PG	5.11	-5.08	-0.39	0.61	0.05	3	GEOMAR	0.019	0.080	0.0011	33.8	403.4	this study
TCX-6	6	252.233	PG	4.78	-6.86	-0.49	0.51	0.10	3	GEOMAR	0.017	1.298	0.0012	239.3	184.4	this study
TCX-7	7	252.226	PG	4.47	-6.04	-0.69	0.31	0.11	3	GEOMAR	0.008	0.067	0.0015	51.0	762.3	this study
TCX-10	10	252.206	PG	4.83	-6.11	-0.76	0.24	0.05	3	GEOMAR	0.013	0.235	0.0014	94.5	402.8	this study
TCX-16	16	252.166	PG	4.04	-6.06	-0.75	0.25	0.20	3	GEOMAR	0.009	0.097	0.0016	50.9	524.6	this study
TCX-18	18	252.152	PG	4.24	-6.43	-0.61	0.39	0.10	3	GEOMAR	0.027	0.195	0.0012	118.2	607.0	this study
TCX-25	25	252.105	PG	4.62	-4.58	-0.76	0.24	0.16	3	GEOMAR	0.018	0.100	0.0012	48.0	467.5	this study
TCX-35	35	252.038	PG	3.77	-5.76	-0.92	0.08	0.01	3	GEOMAR	0.013	0.062	0.0017	53.7	869.1	this study
TCX-37	37	252.025	PG	1.61	-5.94	-0.65	0.35	0.10	3	GEOMAR	0.013	0.067	0.0026	86.2	1287.3	this study
TCX-40	40	252.005	PG	4.09	-5.30	-1.00	0.00	--	3	GEOMAR	0.016	0.073	0.0021	46.7	640.2	this study
TCX-44	44	251.978	PG	2.25	-6.46	-0.82	0.18	0.20	3	GEOMAR	0.005	0.098	0.0016	60.8	618.4	this study
TCX-47	47	251.958	PG	3.61	-5.99	-1.02	-0.02	0.02	3	GEOMAR	0.010	0.185	0.0016	114.7	620.6	this study
TCX-47.5	47.5	251.955	PG	2.98	-5.93	-0.73	0.27	0.02	3	GEOMAR	0.017	0.153	0.0022	83.0	543.6	this study
TK-0.03	46.83	251.959	PG	3.53	-5.79	-0.66	0.34	0.05	3	GEOMAR	0.007	0.126	0.0015	86.4	687.8	this study
TK-1.5	48.3	251.949	PG	2.39	-6.20	-0.79	0.21	0.03	3	GEOMAR	0.011	0.067	0.0021	71.4	1059.6	this study
TK-2.15	48.95	251.945	MW	3.18	-5.81	-0.75	0.25	0.06	3	GEOMAR	0.017	0.143	0.0017	118.8	829.5	this study
TK-2.9	49.7	251.936	TH	-1.29	-6.08	-0.76	0.24	0.05	3	GEOMAR	0.007	0.062	0.0020	61.4	996.2	this study
TK-3.8	50.6	251.925	TH	-0.03	-6.71	-0.96	0.04	0.10	3	GEOMAR	0.008	0.138	0.0012	86.6	627.0	this study
TK-4.15	50.95	251.925	MW	0.44	-6.69	-0.81	0.19	0.09	3	GEOMAR	0.009	0.087	0.0017	76.2	874.7	this study
TK-7.3	54.1	251.921	MW	-0.57	-6.74	-0.70	0.30	0.03	3	GEOMAR	0.005	0.053	0.0030	81.8	1554.8	this study
TK-12.3	59.4	251.916	MW	-0.41	-6.94	-1.05	-0.05	0.01	3	GEOMAR	0.005	0.051	0.0055	134.6	2618.5	this study
TK-18.1	64.9	251.911	MW	-0.89	-7.09	-0.90	0.10	0.15	3	GEOMAR	0.004	0.030	0.0052	80.1	2675.9	this study
TK-27.1	73.9	251.902	OL	-0.50	-7.08	-0.88	0.12	0.10	3	GEOMAR	0.003	0.012	0.0069	45.1	3779.1	this study
TK-34.1	80.9	251.895	OL	-0.54	-7.25	-0.93	0.07	0.06	3	GEOMAR	0.004	0.024	0.0054	69.4	2929.6	this study
TK-40.1	86.9	251.889	OL	-0.52	-7.97	-0.91	0.09	0.03	3	GEOMAR	0.004	0.012	0.0066	39.3	3270.7	this study
TK-45.5	92.3	251.882	OL	-1.25	-7.32	-0.98	0.02	--	3	GEOMAR	0.008	0.104	0.0011	58.2	561.7	this study
TK-47	93.8	251.882	OL	-0.47	-7.70	-1.17	-0.17	0.04	3	GEOMAR	0.007	0.022	0.0024	28.7	1301.0	this study
TK-48.5	95.3	251.880	OL	-0.59	-7.32	-0.71	0.29	0.07	3	GEOMAR	0.008	0.026	0.0056	20.9	811.4	this study
TK-54.5	101.3	251.868	PG	1.01	-7.02	-0.75	0.25	0.05	3	GEOMAR	0.011	0.247	0.0023	276.7	1118.4	this study
TK-58.7	105.5	251.856	PG	2.23	-7.41	-0.56	0.44	0.02	3	GEOMAR	0.005	0.061	0.0051	100.3	1654.3	this study
TK-62	108.8	251.837	PG	0.26	-7.93	-0.45	0.55	0.27	3	GEOMAR	0.009	0.421	0.0044	804.8	1909.5	this study
TK-76.5	123.3	251.755	PG	0.00	-8.19	-0.64	0.36	0.08	2	Berkeley	0.009	0.039	0.0016	20.1	511.7	this study
TK-88	134.8	251.690	PG	0.49	-7.44	-0.70	0.20	0.22	3	Berkeley	0.004	0.160	0.0032	195.2	1208.0	this study
TK-95	142.3	251.648	MW	0.26	-7.42	-0.52	0.48	0.13	3	GEOMAR	0.006	0.113	0.0045	241.8	2130.5	this study
TK-109	155.8	251.572	MW	1.78	-6.65	-0.35	0.65	0.07	3	GEOMAR	0.082	0.134	0.0026	155.9	1163.7	this study
TK-128	174.8	251.464	PG	1.06	-7.15	-0.73	0.27	0.07	2	Berkeley	0.006	0.017	0.0038	18.6	1068.9	this study
TK-136.5	183.3	251.426	PG	1.08	-8.02	-0.54	0.46	0.21	3	GEOMAR	0.003	0.010	0.0042	20.6	2084.5	this study
TK-139.5	186.3	251.417	DL	0.88	-6.23	-0.42	0.48	0.09	1	Berkeley	0.309	0.064	0.0008	14.2	220.8	this study
TK-151	197.8	251.380	PG	1.60	-8.15	-0.13	0.87	0.04	3	GEOMAR	0.005	0.008	0.0028	11.4	1476.1	this study
TK-169	215.8	251.322	PG	0.14	-8.13	-0.57	0.33	0.27	2	Berkeley	0.012	0.744	0.0016	350.2	470.7	this study
TK-176.2	223	251.299	PG	1.31	-7.99	-0.50	0.50	0.00	3	GEOMAR	0.022	0.323	0.0030	463.7	1436.3	this study
TK-201	247.8	251.220	PG	3.32	-7.83	-0.29	0.71	0.11	2	Berkeley	0.051	0.570	0.0009	173.8	302.6	this study
TK-207	253.8	251.201	OL	6.44	-7.74	-0.28	0.72	0.08	3	GEOMAR	0.015	0.660	0.0012	236.4	358.3	this study
TK-226	272.8	251.114	PG	2.04	-8.35	-0.55	0.45	0.20	3	GEOMAR	0.022	0.702	0.0030	568.0	809.2	this study
TK-234	280.8	251.078	PG	0.87	-8.00	-0.79	0.21	0.30	3	GEOMAR	0.016	0.901	0.0024	656.4	728.5	this study
TK-265.5	312.3	250.933	OL	-1.57	-7.98	-0.79	0.11	0.09	3	Berkeley	0.007	0.049	0.0040	54.5	1111.5	this study
TK-287	333.8	250.833	MW	-1.72	-8.01	-0.50	0.50	0.06	3	GEOMAR	0.010	0.066	0.0037	72.6	1095.0	this study
TK-305	351.8	250.750	PG	-0.71	-7.63	-0.79	0.21	0.09	2	Berkeley	0.008	0.068	0.0050	98.4	1437.2	this study
TK-315	361.8	250.294	MW	3.55	-6.76	-0.72	0.18	0.22	3	Berkeley	0.005	0.060	0.0052	120.9	2060.0	this study
TK-321	367.8	249.888	--	0.10	-7.97	-0.73	0.27	0.05	2	Berkeley	0.008	0.111	0.0019	63.5	575.0	this study
TK-351	397.8	249.191	MW	-1.69	-7.27	-0.83	0.07	0.07	3	Berkeley	0.048	0.230	0.0016	134.3	583.4	this study
TK-377.5	424.3	249.004	MW	-0.41	-7.67	-0.50	0.40	0.16	2	Berkeley	0.008	0.130	0.0023	123.5	923.7	this study
TK-450.5	497.3	248.487	MW	-2.01	-7.77	-0.51	0.49	0.22	3	Berkeley	0.010	0.370	0.0027	303.0	817.9	this study
TK-474.8	521.6	248.037	MW	0.38	-3.76	-0.24	0.76	0.06	2	Berkeley	0.363	0.393	0.0011	86.8	220.9	this study
TK-489.5	536.3	247.627	MW	0.96	-2.81	-0.59	0.41	0.13	2	Berkeley	0.020	1.377	0.0016	630.0	457.4	this study
TK-562	608.8	246.568	DL	-1.54	-3.40	-0.53	0.47	0.00	2	Berkeley	0.448	2.708	0.0007	268.5	99.2	this study
TK-627	673.8	246.075	MW	0.33	-6.84	-0.70	0.30	0.02	2	Berkeley	0.008	0.280	0.0013	133.7	483.9	this study
TKU-25	705	245.838	MW	0.63	-5.26	-0.74	0.26	0.10	2	Berkeley	0.016	0.041	0.0043	49.2	1189.5	this study
TKU-63.7	743.7	245.545	MW	0.16	-5.35	-0.49	0.51	0.09	2	Berkeley	0.009	0.029	0.0022	19.4	676.6	this study
TKU-218.:	898.5	244.371	PG	1.46	-7.23	-0.46	0.54	0.06	2	Berkeley	0.035	0.039	0.0022	24.7	628.9	this study

[1] PG = packstone/grainstone; TH = thrombolite; MW = mudstone/wackestone; OL = oolite; DL = dolostone

Table A.1. Regression statistics comparing linear models with log-linear models for the data in this study and for published datasets. ΔAIC is the difference between the

Reference	**Sr data format**	**Linear**					**Log-linear**					**ΔAIC**
		R^2	**p-value**	**AIC**	**slope (± SE)**	**intercept (± SE)**	**R^2**	**p-value**	**AIC**	**slope (± SE)**	**intercept (± SE)**	
Latest Permian - Late Triassic, *this study*	[Sr]	0.303	<0.001	1912.4	-0.0005 ± 0.0000	-0.1239 ± 0.0368	*0.458*	*<0.001*	*10.1*	*-0.7479* ± *0.0354*	*1.533* ± *0.1340*	-1902.4
	Sr/Ca	*0.313*	*<0.001*	*-1404*	*-227.3* ± *18.51*	*-0.0455* ± *0.0413*	0.440	<0.001	-47.0	-0.9637 ± 0.0706	-3.217 ± 0.1913	1356.8
	Sr/(Ca+Mg)	0.328	<0.001	155.3	-0.4740 ± 0.0376	-0.0704 ± 0.0388	*0.460*	*<0.001*	*-12.0*	*-0.8172* ± *0.0575*	*-0.6557* ± *0.0266*	-167.2
Triassic/Jurassic, *Jost et al. (2017)*	[Sr]	0.574	<0.001	460.4	-0.0003 ± 0.0000	-0.3558 ± 0.0597	*0.565*	*<0.001*	*-32.9*	*-0.8370* ± *0.1201*	*1.783* ± *0.3239*	-493.3
	Sr/Ca	*0.578*	*<0.001*	*-334.4*	*-106.6* ± *15.05*	*-0.3250* ± *0.0625*	0.548	<0.001	-34.2	-0.8712 ± 0.1277	-2.923 ± 0.2870	300.2
Permian/Triassic, Silva Tamayo et al., in review (Oman and Italy)	[Sr]	0.362	<0.001	515.5	-0.0008 ± 0.0001	-0.2139 ± 0.0803	*0.541*	*<0.001*	*58.4*	*-0.5607* ± *0.0781*	*0.6741* ± *0.1556*	-457.1
	Sr/Ca	*0.342*	*<0.001*	*-389.5*	*-400.6* ± *66.94*	*-0.1704* ± *0.0831*	0.634	<0.001	5.0	-1.067 ± 0.1290	-4.021 ± 0.3886	394.5
Middle - Late Permian, *Jost et al. (2014)*	[Sr]	0.004	0.65	586.4	-0.0006 ± 0.0001	-0.0491 ± 0.0660	*0.003*	*0.69*	*-104.0*	*-0.8267* ± *0.1431*	*1.840* ± *0.3443*	-690.4
	Sr/Ca	*0.002*	*0.75*	*-652.9*	*-251.8* ± *43.61*	*-0.0209* ± *0.0700*	0.000	0.90	-108.7	-0.8694 ± 0.1507	-2.887 ± 0.3741	544.2
	Sr/(Ca+Mg)	0.001	0.81	-64.9	-0.5509 ± 0.0955	-0.0267 ± 0.0693	*0.000*	*0.96*	*-107.4*	*-0.8581* ± *0.1488*	*-0.5787* ± *0.0414*	-42.5
Late Silurian, *Farkas et al. (2016)*	[Sr]	0.490	<0.001	402.8	-0.0014 ± 0.0002	0.1356 ± 0.0899	*0.540*	*<0.001*	*-103.3*	*-1.467* ± *0.1975*	*3.377* ± *0.4722*	-506.1
	Sr/Ca	*0.669*	*<0.001*	*-517.4*	*-391.9* ± *44.07*	*0.1963* ± *0.0781*	0.699	<0.001	-123.5	-1.571 ± 0.1676	-4.854 ± 0.4220	394.0
Late Ordovician, *Holmden et al. (2012a)*	[Sr]	0.226	0.004	431	-0.0003 ± 0.0001	-0.1630 ± 0.0500	*0.172*	*0.01*	*-74.2*	*-0.5759* ± *0.1116*	*1.208* ± *0.2746*	-505.2
Ordovician, *Holmden (2009)*	Sr/Ca	*0.799*	*<0.001*	*-208.7*	*1377* ± *187.6*	*-0.9522* ± *0.0874*	0.804	<0.001	-36.3	1.0346 ± 0.1396	3.150 ± 0.5746	172.4
Ediacaran, *Husson et al. (2015)*	[Sr]	0.129	<0.001	4429.8	-0.0002 ± 0.0000	-1.114 ± 0.0273	*0.403*	*<0.001*	*126.3*	*-0.6889* ± *0.0351*	*0.6079* ± *0.0968*	-4303.5
Ediacaran, Sawaki et al. (2014)	[Sr]	0.174	0.002	917.2	-0.0002 ± 0.0000	-0.0994 ± 0.0426	*0.199*	*<0.001*	*30.0*	*-0.5003* ± *0.0706*	*1.018* ± *0.1605*	-887.1
Modern, *Fantle and Higgins (2014)*	Sr/(Ca+Mg)	0.372	0.04	12.8	-0.1790 ± 0.0643	0.1519 ± 0.0698	*0.151*	*0.21*	*0.21*	*-0.3520* ± *0.1511*	*-0.1328* ± *0.0845*	-12.6
Compilation of all data	[Sr]	0.130	<0.001	10309	-0.0002 ± -0.0003	-0.2265 ± 0.0167	*0.346*	*<0.001*	*328.9*	*-0.6466* ± *0.0217*	*1.310* ± *0.0584*	-9979.9
	Sr/Ca	*0.302*	*<0.001*	*-3175*	*-196.3* ± *10.19*	*-0.1376* ± *0.0246*	0.317	<0.001	-10.56	-0.8144 ± 0.0418	-2.845 ± 0.1165	3164.1
	Sr/(Ca+Mg)	0.231	<0.001	203.8	-0.4785 ± 0.0330	-0.0404 ± 0.0332	*0.347*	*<0.001*	*-32.0*	*-0.8281* ± *0.0524*	*-0.6150* ± *0.0234*	-235.8